

Constructing a Survey of the Local Interstellar Medium Using Hubble Spectra

by

Fallon P Konow
Class of 2020

A thesis submitted to the
faculty of Wesleyan University
in partial fulfillment of the requirements for the
Degree of Bachelor of Arts
with Departmental Honors in Astronomy

Abstract

Light from distant objects transverses through interstellar clouds comprised of warm, partially ionized gas causing extinction. The Sun itself is embedded in a complex amalgamation of these clouds known as the Local Interstellar Medium (LISM). Observations using the Space Telescope Imaging Spectrograph (STIS) aboard the *Hubble Space Telescope* have provided high resolution near ultraviolet (NUV) spectra showing MgII, FeII, and in some cases, MnII absorption due to the LISM. Spectra were analyzed for the sightlines towards 34 stars within 100 parsecs spanning the entire sky. The heavy ions studied in this survey produce narrow absorption features, making the identification of multiple LISM components within an individual sightline possible. Simultaneous fits of the MgII and FeII doublets show anywhere from one to five discrete absorption features per sightline. Furthermore, characteristics of the absorption features (centroid, width, and depth) reveal the physical parameters (radial velocity, Doppler parameter, and column density) of the clouds themselves. The majority of the components identified are well correlated to previous LISM studies conducted by Redfield & Linsky in 2008 and Malamut et al. in 2014, 13 sightlines show evidence for previously unidentified clouds within the LISM. These measurements will add to a growing data set of 191 NUV sightlines probing the LISM. The addition of the 34 sightlines in this survey will test and refine the current dynamical model of the LISM. Additionally, many of the sightlines analyzed in this survey have been previously observed and analyzed in the far UV, providing lighter ion fits for LISM. This information combined with the heavy ion fits from this survey will provide constraints which allow the measurement of additional physical properties of the LISM such as temperature, turbulence, abundances, and depletion.

Code 7

VVO BASEMENT

2020

Acknowledgements

I would like to acknowledge the support for this project through NASA HST Grant GO-13332 awarded by the Space Telescope Science Institute, which is operated by the Association of Universities for Research in Astronomy, Inc., for NASA, under contract NAS 5-26555, a student research grant from the Wesleyan Math and Science Scholars (WesMaSS), and well as a student research fellowship from the Connecticut Space Grant Consortium. Thank you for giving me the opportunities to pursue research.

In addition to these large supporters, there are so many individuals who have played such an important role in my success that I would like to thank. I am extremely grateful to the entire astronomy department for their support and encouragement throughout my time at Wes. So that I do not write an acknowledgments section just as long as my thesis itself, I have created a short list of people I would like to thank for helping me, specifically with my thesis. To everyone I do not individually name but who have been there for me through every step of this process, know that I am eternally grateful for everything you have done.

To my advisor Seth Redfield: Thank you for your academic guidance during my entire career at Wesleyan and your undying support in my research these past two years. Your enthusiasm for all things astronomy in ASTR155 my freshmen year solidified my choice to major in astronomy and physics, while your undying patience and tutelage these past few years has helped me grow as a student and researcher. You have broadened my horizons and skills; I cannot thank you enough for everything you have done for me.

To my partners in crime Gil and Hunter: Thank you for being by my side every step of the way and putting up with my ridiculousness. You have both been

such strong influences in my life, and I cannot imagine my time at Wes without you two. Gil, thank you for always being ready to answer my questions no matter how stupid they may be. You have saved me and my assignments more times than I can count. Hunter, thank you for pushing me to start research and join Seth's group – without you, there is no telling if I would even be working on this project right now. You have been such an integral part of my research success.

To Ben, Kim, the rest of Rogue, and the entire VVO basement: Thank you for being the most amazing friends. Your silliness and support have gotten me through even the worst of times. You have become a second family to me, and I will dearly miss seeing your faces everyday. My life would be horribly boring without you in it.

Finally, to my loving family: Thank you for being my biggest fans and always listening to my research-related ramblings even when you had absolutely no idea what I was talking about. Thank you for always believing in me and boosting my confidence especially when I did not believe in myself. Even from hundreds of miles away, your unconditional love and support give me the courage to go after my dreams and reach new heights. Audrey, thank you for being my other half and always standing by my side (quite literally for the past 21 years). You give me the strength to do things I would never think possible otherwise.

Contents

1	Introduction	1
1.1	The Local Interstellar Medium	2
1.1.1	Observing and Categorizing the LISM	3
1.2	Past ISM Studies	5
1.2.1	Initial ISM Observations	5
1.2.2	HST and Past SNAP Surveys	6
2	Observations and Data Reduction	9
2.1	A SNAP Survey with STIS	9
2.1.1	STIS	10
2.1.2	A SNAP Survey	11
2.2	Data Reduction	15
3	Fitting	16
3.1	Fitting Procedure	16
3.1.1	Pre-Fitting Analysis	17
3.1.2	Fitting the Continuum	19
3.1.3	Fitting the ISM Absorption	21
3.1.4	Uncertainty and Error	24
3.2	Fits	26
3.3	Final Fit Parameters	45
3.3.1	Upper Limits	46

4	Results and Analysis of Sample	50
4.1	The Velocity Distribution	51
4.2	The Doppler Parameter Distribution	52
4.3	The Column Density Distribution	54
4.4	Multi-Component Fits and Distance	55
5	Discussion	58
5.1	Comparison to Kinematic Model	58
5.1.1	Previously Unidentified Clouds	61
5.1.2	Small Scale Structure	63
5.2	Depletion	65
5.3	Temperature and Turbulence	66
5.4	Ly α Emission and Astrospheres	68
6	Conclusion	71
6.1	Future Work	72
	Bibliography	74

Chapter 1

Introduction

The stars within our galaxy are embedded in a complex system of gas and dust clouds known as the interstellar medium (ISM). The region containing our solar system and the surrounding 100 pc is denoted as the Local Interstellar Medium (LISM). The blanketing presence of these clouds means that whenever we observe objects outside of our solar system, we must first peer through the LISM. The gas and dust present in the LISM clouds absorb and scatter stellar emission, making the proper identification of these clouds crucial to fully understanding the stars behind them.

The importance of understanding the LISM extends beyond absorption corrections for stellar observations. Being embedded in these clouds means our solar system is directly interacting with the LISM. As the Sun moves through its orbit in the galaxy, the balance of pressure between the outward pointing solar wind and the inward interaction of the ISM clouds defines the boundary, known as the heliopause, between the solar system and the rest of the universe (Wyman & Redfield 2013). Due to the motion of both the solar system and the ISM clouds, the heliopause is a dynamic boundary whose location and existence can have direct effects of planets and their atmospheres (Usoskin et al. 2005; Pavlov et al. 2005).

The origin of the LISM clouds is closely related to the the origins and development of our local interstellar environment (Breitschwerdt et al. 2000). This

insight combined with our understanding of the heliosphere and the ISM helps reveal to us the history of our local solar neighborhood. The knowledge of these clouds also provides insights into the general ISM. We can extend our model of the small-scale structure of the LISM to similar, more distant regions of the ISM, potentially allowing us to better understand the interstellar workings of our galaxy.

1.1 The Local Interstellar Medium

The LISM is an agglomeration of discrete gas and dust clouds which can be found in different phases. McKee & Ostriker determine in their 1977 paper (McKee & Ostriker 1977) that, assuming pressure equilibrium, the interstellar medium exists in three phases: hot ionized medium (HIM), cold neutral medium (CNM), and intermediary warm medium (both neutral: WNM and partially ionized: WIM). The HIM phase fills the largest portion of interstellar space; its temperature is as high as $T \sim 10^6$ K and its density is as low as $n \sim 10^{-2.5} \text{ cm}^{-3}$. CNM regions are embedded in the HIM and are surrounded by the WNM and WIM. The CNM is much denser than the HIM with a density of $n \sim 100 \text{ cm}^{-3}$ and much cooler temperatures closer to $T \sim 100$ K. The presence of WNM or WIM ($T \sim 8000$ K, $n \sim 0.5 \text{ cm}^{-3}$) depends on the heat source shielding in that region, but is always found surrounding the CNM (McKee & Ostriker 1977).

Our solar system currently lives in a large, blown-out region of the HIM named the Local Bubble that was most likely created by supernova and stellar winds (Frisch & York 1983). Its existence was first suggested by color excess maps that indicated a large pocket in dust surrounding the solar system and the presence of a soft x-ray background that stretches across the sky (Frisch et al. 2011). The

edge of the Local Bubble is found anywhere from 65–250 pc (depending on the direction), and was determined through the analysis of NaI and CaII absorption (Sfeir et al. 1999). Figure 1.1 depicts the edges of the Local Bubble and its surrounding CNM regions as determined by Lallement et al. (2003). Since the Local Bubble extends farther than 100 pc along most lines of sight, the vast majority of LISM observations in this survey are of clouds in the Local Bubble.

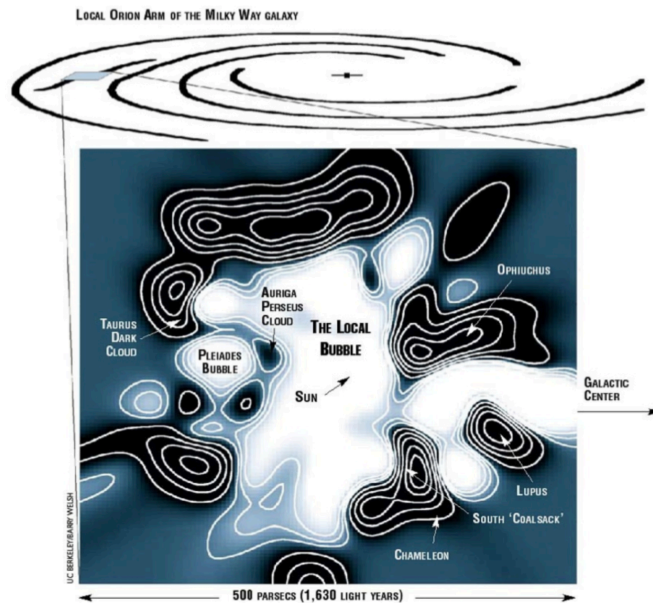


Figure 1.1: A map of the ISM near the Sun indicating the Local Bubble and surrounding regions (Lallement et al. 2003). The Local Bubble (HIM) is presented in white while the surrounding black regions show the CNM.

1.1.1 Observing and Categorizing the LISM

Despite the fact that a majority of our observed LISM clouds reside in the HIM of the Local Bubble, these clouds are not hot enough to be emissive. Because of this, the most direct way to observe LISM clouds is through their absorption of bright background stars' spectra. The position, width, and depth of the ab-

sorption features correspond to physical parameters unique to each cloud. This method of observation not only allows us to distinguish discrete clouds from one another, but also gives us the means to learn about individual cloud properties. In order to do this kind of observation, space-based observatories like the *Hubble Space Telescope* (*HST*) are necessary because the most common ion resonance lines in the ISM exist in the UV (Malamut et al. 2014). The creation of high-resolution spectrographs on *HST* has allowed the study of LISM to develop with great precision.

Because of their relatively strong atomic transitions and relatively high abundance in the LISM (Slavin & Frisch 2008), we preferentially choose to investigate heavier elements like the ions, MgII, FeII, and MnII in our search for LISM features (Malamut et al. 2014). These ions' relatively high masses reduce the thermal broadening of their features (Frisch et al. 2011) which allows for individual clouds along a single line of sight to be more easily discerned. Additionally, these ions have the benefit of being multiplets (having more than one ground state transition) which, for each sightline, provides multiple independent fits for each absorption feature. This provides a more precise measurement of individual cloud properties.

When attempting to observe ISM clouds that reside at distances of hundreds or thousands of parsecs away, absorption lines of the ions in the ISM can often be blended or saturated (Wyman & Redfield 2013), making it difficult to discern individual components. Observing nearby (< 100 pc) stars and ISM clouds provides sharper absorption features that are less likely to be blended and lead to better determinations of LISM components. Assuming a Copernican Principle, our study of the nearby LISM allows us to extend our understanding of the galactic ISM as a whole.

1.2 Past ISM Studies

1.2.1 Initial ISM Observations

Although not always called the interstellar medium, the idea of the presence of material residing between stars, absorbing light has existed for over a century. One of the first indications of interstellar absorption was presented by Hartmann in his 1904 paper which studied the spectroscopic binary system δ Orionis. In his paper, he notes the observation of an unmoving calcium feature present among the oscillating lines of the binary system. He determined that the CaII spectral line must have been caused by calcium gas existing between the observer and δ Orionis. Another study on δ Orionis completed by Heger in 1919 confirmed the presence of the calcium line and additionally presented the presence of sodium lines indicative of interstellar gas.

The strong transitions exhibited by calcium and sodium continue to be used in ISM studies (e.g. Beals (1936); Lallement & Bertin (1992); Wyman & Redfield (2013)). Investigation into the CaII line persists in modern survey observing (Redfield & Linsky 2002), but is now supplemented with the investigation of heavier elements like magnesium and iron thanks to space-based facilities. Redfield & Linsky (2008) produced a dynamical model of the LISM through the analysis of 157 individual sightlines' heavy element absorption. Along with their publication, they created a Kinematic Calculator¹ which gives predictions of LISM cloud presence and radial velocity along a given sightline. This work was furthered by Malamut et al. (2014) who added an additional 34 sightlines to the model.

¹<http://lism.wesleyan.edu/LISMdynamics.html>

1.2.2 HST and Past SNAP Surveys

The identification of interstellar gas and dust may have occurred nearly a century ago, but it is only recently, thanks to space-based spectroscopic observatories that we are able to study it in great detail. With the launch of the *International Ultraviolet Explorer (IUE)* in 1978 and *HST* equipped with the Goddard High-Resolution Spectrograph (*GHRSS*) in 1990, investigation into UV spectra of stars in search of ISM became possible. Investigations by Genova et al. (1990) using *IUE* indicated the discrete cloud nature of the LISM, although were unable to resolve the clouds beyond the “Local Cloud” due to the coarse spectral resolution of the *IUE*. Subsequently, Lallement and Bertin combined observations of the CaII lines of 6 stars toward the galactic center using the Aurèlie spectrograph at the L’Observatoire de Haute-Provence with the projected velocity vector onto the α Aur direction as obtained by the GHRSS in Linsky et al. (1993). They identified the two nearest LISM clouds, named the Local Interstellar Cloud (LIC) and the Galactic Cloud (G) (Lallement & Bertin 1992).

Then in 1997, Hubble’s update from GHRSS to STIS (the Space Telescope Imaging Spectrograph) increased the telescope’s spectral capabilities through the implementation of high performance digital cameras and read out modes which give it the ability to capture broad spectral coverage in a single echelle exposure (Ayres 2010). STIS can achieve a maximum spectral resolution of $R \sim 114000$ over the spectral range 1150–3100 Å (Ayres 2010) as compared to GHRSS’s maximum resolution of $R \sim 80000$ over the range 1150–3200 Å ($R = \frac{\lambda}{\Delta\lambda}$). STIS continues to be the premiere instrument for high-resolution UV spectroscopy, and its vast capabilities have been implemented by many to study the LISM.

Redfield & Linsky (2002) used the capabilities of STIS to continue observations

like Lallement & Bertin (1992), developing the technique to further study the LISM through the analysis of MgII and FeII lines. Their various investigations lead to the identification and characterization of 15 discrete clouds as seen in Figure 1.2 (Redfield & Linsky 2004, 2008). Findings of the Redfield & Linsky (2008) survey motivated the work of Malamut et al. (2014) who presented an additional large survey which refined and extended the LISM measurements. The increased sky coverage with each additional survey further refines and improves our model of the LISM, but it also indicates the need for additional investigation. The goal of this survey is to contribute an additional large sample of LISM measurements through the observation of heavy elements like MgII, and FeII to further refine the LISM dynamical model.

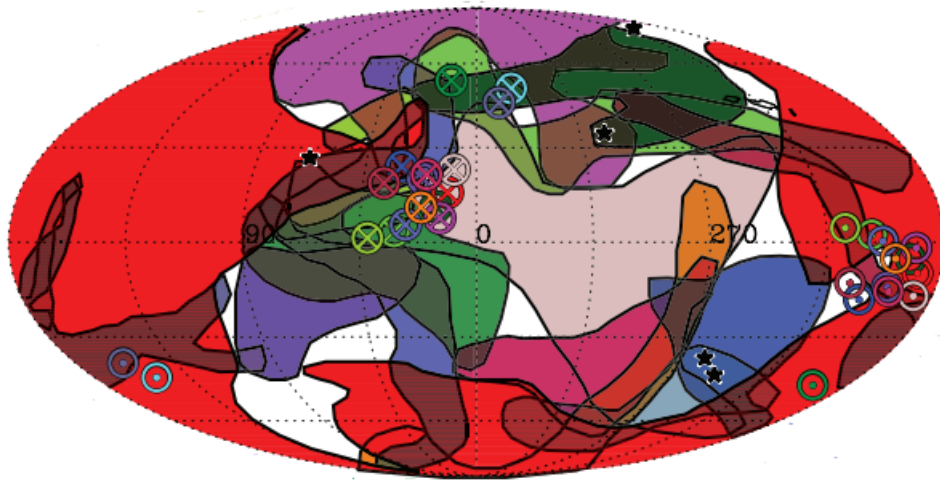


Figure 1.2: The boundaries of 15 LISM clouds determined through the analysis of 157 stars within 100 pc (Redfield & Linsky 2008). The circled \times denotes the heliocentric upwind velocity of clouds while the circumpunct denotes the downwind direction. The black stars are sight lines of radio scintillation sources identified by Linsky et al. (2008).

Because the LISM is so dynamic on small scales, full sky coverage is necessary in order to produce a truly comprehensive model of the LISM. Previous studies by Redfield & Linsky (2008) and Malamut et al. (2014) have analyzed 191 individual sightlines, identifying 15 individual clouds. The addition of 37 targets in this study increases the total number of sightlines analyzed for ISM absorption by nearly 20%, and probes new regions of the sky not yet analyzed. The goal of this survey is to contribute additional observations to broaden the scope of and refine the measurements of the dynamical LISM model. We do this in order to better understand our solar neighborhood and the interstellar workings of our galaxy as a whole.

Chapter 2

Observations and Data Reduction

2.1 A SNAP Survey with STIS

The data used in this survey were obtained from a Snapshot (SNAP) survey by the *Hubble Space Telescope's* (*HST*) Space Telescope Imaging Spectrograph (STIS). The SNAP survey is designed to productively utilize all of *HST's* observing time (Section 2.1.2). STIS produces high resolution ($R \equiv \frac{\lambda}{\Delta\lambda} \sim 114000$) spectra in the UV band (1140–3100 Å). Since ISM clouds are non-emitting bodies which have low optical depth, they can only be detected through spectral analysis of their absorption features. UV wavelengths are ideal for this sort of observation because of the particular ion emission lines present in these bands. MgII (2796.3543 Å and 2803.5315 Å) and FeII (2586.6500 Å and 2600.1729 Å), the main ions investigated in this survey, were chosen because they are particularly abundant in the LISM and their gas phase abundances can be treated as parameters that vary directly with the cloud's total column density (Slavin & Frisch 2002). Additionally, they have relatively strong atomic transitions resulting in strong emission lines in these desired wavelength range (Figure 2.1).

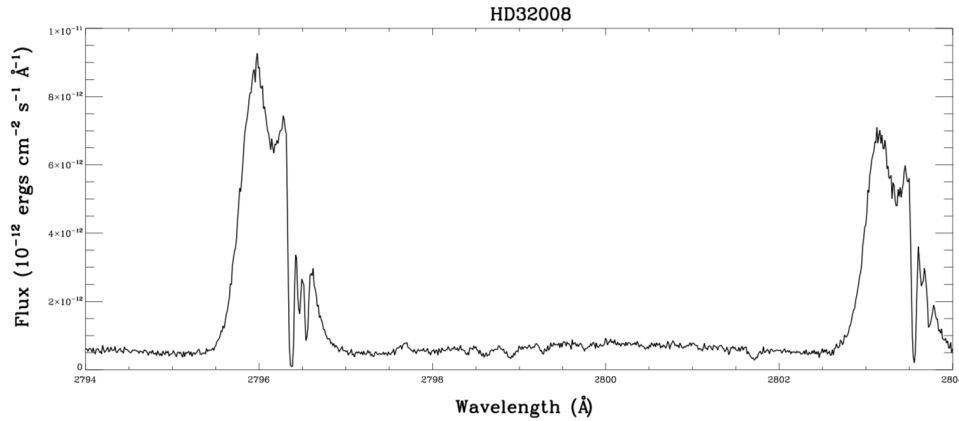


Figure 2.1: A portion of the spectrum of HD32008 obtained by STIS. Strong stellar emission features of MgII can be seen at 2796.3543 Å and 2803.5315 Å with clear ISM absorption on the redder side of each emission feature.

2.1.1 STIS

STIS provides spatially resolved spectra for wavelength ranges of 1150–10300 Å. It operates with 3 detectors: a CCD and two Multi-Anode Microchannel Array (MAMA) detectors with fields of view 52 x 52 arcseconds and 25 × 25 arcseconds respectively. The MAMA has both a FUV-MAMA (far-UV) and a NUV-MAMA (near-UV). The NUV-MAMA’s wavelength range is 1600-3100 Å and is the detector that was used for this survey. It was chosen because of its two-dimensional UV imaging capabilities, high spatial resolution, and low background for point sources (Bostroem & Proffitt 2011).

In order to obtain high spectral resolution, the spectrograph’s E230H (echelle) grating is used in conjunction with the NUV-MAMA. This grating provides spectra with a maximum resolving power $R \equiv \frac{\lambda}{\Delta\lambda} \sim 114000$ within the range of 1620–3150 Å. The E230M grating’s sensitivity peaks near 2600 Å, which is ideal for the analysis of our chosen ions MgII (2796.3543 Å and 2803.5315 Å), FeII (2586.6500 Å and 2600.1729 Å). E230H grating produces spectra in orders separated by dif-

ferent wavelength ranges that are then combined to make one complete spectrum.

Figure 2.2 presents the raw spectral data obtained for target HD32008.

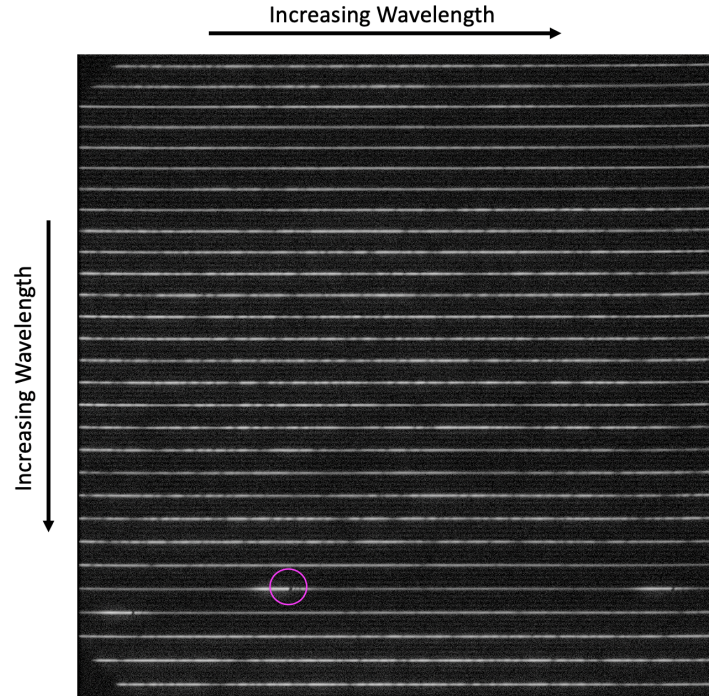


Figure 2.2: An example of the raw data of HD32008. Each row represents a different order of E230H echelle observation. The spectrum in its entirety increases in wavelength from left to right and from top to bottom. The brighter white portions represent stellar emission and the dark patches within represent ISM absorption. The circled feature represents the absorption by the 2796.3543 Å line of MgII.

2.1.2 A SNAP Survey

Since this study aims to contribute to and develop an all sky survey of the LISM clouds, it is ideal to obtain a randomized distribution of observations. Designed as a way to maximize productive observing time by allowing short exposures of certain targets in between other, more time intensive observations, a SNAP Survey provides the ideal means to do this. These observations are limited to less than 45 minutes, including 20 minutes of preparation time, resulting in 25 minute

exposures for each target (Bostroem & Proffitt 2011). The observed targets are chosen randomly out of a larger proposed list of targets with an expected return rate $\sim 30\%$. For this particular survey, 70 targets within a distance of 100 pc were proposed, and 37 ($\sim 53\%$) were observed.

This survey was awarded in Cycle 21, Proposal ID 13332 (Redfield 2013). These 70 targets were proposed based on their moderate or high resolution spectrum already observed by *HST* or the *Far Ultraviolet Spectroscopic Explorer* (*FUSE*). Having observations in both the FUV and NUV allows for temperature and turbulence analysis of individual clouds. Analyzing the absorption of heavier elements, like MgII and FeII, also helps constrain Ly α fits, providing possible insight into the astrospheres of stars (Section 5.4). These targets were also chosen to be widely scattered throughout the sky with the goal of broadening the current dynamical model’s reach.

The final spectra of the survey had an average S/N of 9.2 and 4.8 for MgII and FeII respectively. The S/N was calculated by averaging eh flux divided by its error for the range of $\sim \pm 40$ km s $^{-1}$ surrounding each emission line. Since this range contains the absorption feature, these calculations are likely underestimates. See Table 2.1 for a full list of observed targets. All stellar parameters were taken from the SIMBAD¹ database with the exception of the stellar radial velocities of WD211-495 (Preval et al. 2019) and BD+28D4211 (Greenstein 1952). Additionally, all but 4 targets (WD6044+376, WD0227+050, HD83443, and HD2740) have been previously observed using various other STIS gratings (e.g. 140H, 140M, G430L), so, for brevity, STIS is not listed under the "Other Spectra" column for any of the targets.

¹<http://simbad.u-strasbg.fr/simbad/>

Table 2.1: Parameters for Stars in LISM SNAP Program

HD No.	Other Name	Spectral Type	m_V (mag)	v_R (km s ⁻¹)	Distance (pc)	l (deg)	b (deg)	S/N (MgII)	S/N (FeII)	Other Spectra
201091	61 Cyg A	K5V	5.21	-65.7	3.5	82.32	-5.82	0.1	0.1	COS/ GHRS
33793	VZ-PIC	M1VI	8.853	245.2	3.9	250.53	-36	0.03	0.1	ACS/ COS
191408	HIP99461	K2.5V	0.32	-129.3	6	5.23	-30.92	2.5	3.1	
	GJ436	M3V	10.613	9.6	9.8	210.54	74.57	1.7	0.03	COS
17925	ϵ -ERI	K1V	6.05	17.8	10.4	192.07	-58.25	14.3	4	FUSE/ GHRS
13445	HIP10138	K1.5V	6.17	55.2	10.8	275.93	-61.96	11.46	2.5	COS
37394	HIP26779	K1	6.23	1.3	12.3	158.38	11.95	11.5	3.1	
9826	ν -AND	F9V	4.1	-28.6	13.5	132	-20.67	16.4	9.8	FUSE
166	HR8	G8	9.55	-6.6	13.8	111.26	-32.83	11.5	3.8	FUSE
43162	HIP29568	G6.5V	6.366	21.9	16.7	230.85	-18.52	11.4	3.5	FUSE
	WD0644+376	DA2.3	11.717	80	17.1	178.29	15.42	6.9	7.6	FUSE
165185	HIP88694	G1V	5.95	15	17.2	356.04	-7.33	12.9	4.9	
82443	DX-LEO	G9V	7.155	7.9	18.1	201.21	46.06	9.3	2.6	GHRS
82558	LQ-HYA	K1Vp	7.891	6.2	18.3	244.59	28.4	11.5	3.2	GHRS
203244	HIP105712	G5V	6.97	11.5	20.8	324.9	-38.91	13.4	4.8	
199288	GJ9712	G2V	6.52	-7.9	21.6	356.69	-40.68	4.7	2.2	COS
116956	HIP65515	G9V	7.379	-12.1	21.7	113.7	59.54	8.4	2.1	
59967	HIP36515	G3V	6.635	9.4	21.8	250.45	-8.97	9.5	3.2	
	GJ9124	G1-2V	10.4	5.6	22.1	165.58	-23.42	2.6	0.8	COS/ FOS/ GHRS
128987	HIP71743	G8V	7.24	-22.9	23.8	337.54	39.22	11	2.7	
	CD-34D7151	K6V	10.5	12.3	23.8	278.68	22.95	11.5	3	
73350	V401 Hya	G8/K0(IV)	6.725	35.4	24.3	232.08	19.98	11.4	3.6	
	WD0227+050	DA2.5	12.798	-5.7	26.5	163.04	-49.75	4.6	5.1	
129333	EK Dra	G1.5V	7.604	-20.3	35.8	105.52	49.04	11.7	3.8	COS/ FUSE/ GHRS
26462	45 Tau	F4V	5.699	37.3	37.5	186.58	-31.72	11.5	14.7	COS/ FUSE/ GHRS
83443	HIP47202	K0K0/1V+G(III)	8.24	28.9	40.9	269.6	6.68	4.6	0.9	FUSE
283654	DF Tau	M3V	11.42	12	45.9	172.15	-15.94	7.4	1.4	COS/ FUSE
27901	HIP20614	F4V	5.965	31.7	46.4	177.12	-20.68	20.5	16.2	FUSE
209458	V376 Peg	F9V	7.63	-15	48.4	76.75	-28.53	4.2	2	FUSE
	WD2111+498	DA1.3	13.09	94	50.4	91.37	1.13	3.3	5.5	FUSE/ GHRS
32008	63 Eri	G4IV-V+DA	5.39	-15.8	52.9	209.55	-29.41	29.4	10.6	FUSE
	WD2211-495	DA.7	11.57	25.4	58.9	345.79	-52.62	9.4	11.6	FUSE
240764	RW Aur	K1+K5	9.6	15	64.9	174.2	-6	14.6	2.7	COS
18812	HIP97962	sd	10.22	26.7	73.1	12.63	-25.43	7.8	12.5	
33959C	14 Aur C	F2V+DA1.3	7.88	-8.4	81.7	173.3	-3.36	3.4	2.5	FUSE/ GHRS
160365	HIP86373	F6III	6.123	8.1	99.3	37.09	21.99	5.6	3.9	FUSE
	BD+28D4211	sd	10.58	-12	113.6	81.87	-19.29	8.9	15.1	

This survey builds off of a previous SNAP survey of the LISM (Cycle 17, Proposal ID 11568 Redfield (2009)) which observed 36 different sightlines. 34 of which were successfully fit for MgII absorption and 33 were fit in FeII (with a few MnII detections as well). These results are presented by Malamut et al. (2014). Figure 2.3 depicts the location (in galactic coordinates) of targets in this survey along with the 199 targets from previously/concurrently conducted LISM studies (Redfield & Linsky 2008; Malamut et al. 2014; Vannier 2020).

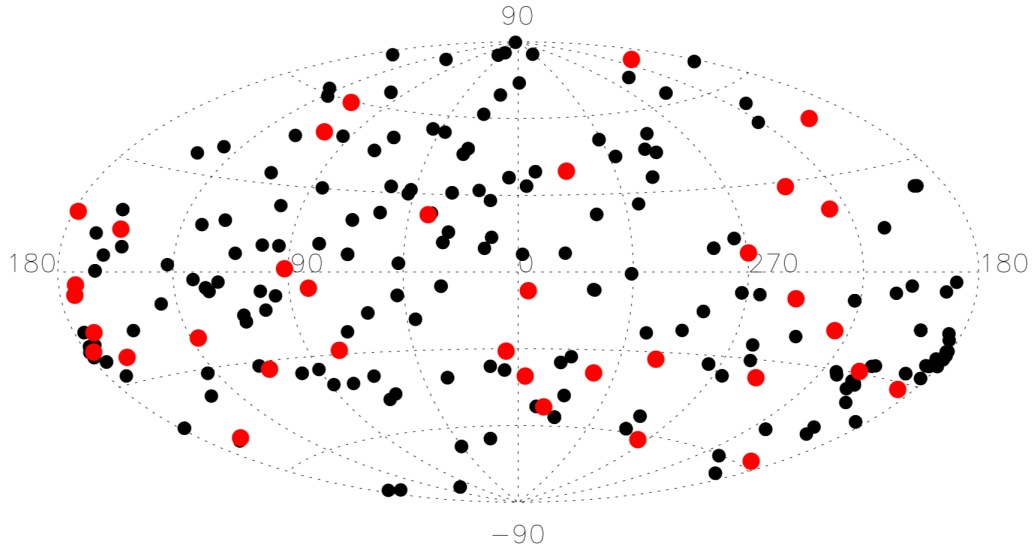


Figure 2.3: A map in galactic coordinates of all sightlines whose spectra have been analyzed for ISM absorption. The black points indicate sightlines studied by Redfield & Linsky (2008), Malamut et al. (2014), and Vannier (2020). The red points indicate the sightlines added with this survey. For the first time, this survey probes the region of the sky near $225^\circ \leq l \leq 270^\circ$ and $0^\circ \leq b \leq 90^\circ$. This survey also contributes multiple new sightlines to the $135^\circ \leq l \leq 225^\circ$ and $-45^\circ \leq b \leq 0^\circ$ region, motivating further analysis into the small-scale structure of the LISM.

2.2 Data Reduction

The NUV-MAMA is a photon-counting detector that produces a two-dimensional UV image; all of the E230H echelle orders are stacked vertically in order of increasing wavelength. The wavelengths at the end of the orders overlap in order to ensure a complete continuous spectra. Figure 2.2 shows an example of the raw data for HD32008. The dark regions within the light continuum are caused by interstellar absorption lines.

Once a spectrum has been obtained, it is received by the Space Telescope Data Capture Facility and sent to the STScI (Space Telescope Science Institute) pipeline **calstis** which unpacks the data, performs linearity correction, flat field correction, and dark and bias subtraction. Additionally, it flags cosmic rays and bad pixels and converts the spectrum to a heliocentric reference frame (Bostroem & Proffitt 2011). In order to convert translate pixels to wavelengths, internal Pt-Cr/Ne line lamps are used to provide a reference spectrum for calibration.

The pipeline produces a two-dimensional, flux-calibrated, spectroscopic image with distance along the slit running linearly along the Y axis and wavelength running linearly along the X axis. From this image, one-dimensional spectra of flux versus wavelength are extracted, so that the final data files used for analysis take the form of binned calibrated FITS files containing arrays of flux, wavelength, and error (Figure 2.1).

Chapter 3

Fitting

3.1 Fitting Procedure

Once the data is collected and reduced, the fitting procedure can begin. Because the LISM varies so greatly even over small distance scales, there is not one blanket method to automatically fit all sightlines in the survey. Factors such as stellar radial velocity offset, number of individual cloud components, and saturation level of absorption features require each sightline to be analyzed and fit individually. Furthermore, one of the first and most integral steps in the fitting procedure, recreating the assumed stellar flux background, is a process for which human input is highly valued and necessary.

Because of their strong stellar emission features and relatively high, absorption-causing abundance in the LISM, the ion doublets MgII and FeII are investigated for each of the 37 sightlines in the survey. For each of these doublets, if the signal-to-noise ratio is high enough, there are 3 independent fitting procedures applied to each sightline per ion. The individual wavelength features of each doublet are fitted separately, and then an additional simultaneous fit of the doublet is carried out. This process produces final fit parameters of radial velocity, column density, and a Doppler parameter for each LISM component. In the case of a low signal-to-noise feature, where components cannot be fit, an upper limit can be calculated

for the column density of a cloud based off of other ions' fits for that sightline. Although some steps change minutely from sightline to sightline and doublet to doublet, the fitting procedure remains vastly the same for every feature.

3.1.1 Pre-Fitting Analysis

Prior to analyzing the spectra, the parameters of the each sightline's stellar features are determined in order to distinguish stellar features and ISM features from each other. Using the survey data and the SIMBAD database, each target star's radial velocity, distance, and galactic longitude and latitude are established (Table 2.1); these values are then used along with Redfield and Linsky's LISM Kinematic Calculator (Redfield & Linsky 2008) to identify any ISM clouds that are predicted to be present along a particular sightline.

In order to identify absorption features indicative of LISM, spectral wavelength values are converted to velocities using the Doppler shift equation. Since ion emission from the stellar atmosphere occur at very particular, discrete wavelengths, when these wavelengths are converted to velocities, the stellar features occur exactly at the radial velocity of the star itself. Therefore, any absorption features found at any other velocity, cannot be indicative of a stellar feature and may be from an ISM component along the sightline. Additionally, the fact that, regardless of wavelength, all stellar emission features will line up with the stellar radial velocity makes translating the spectra from wavelength space to velocity space is advantageous for absorption fitting. Figure 3.1 depicts a velocity space spectrum for HD32008 with its stellar radial velocity and predicted ISM cloud radial velocities identified.

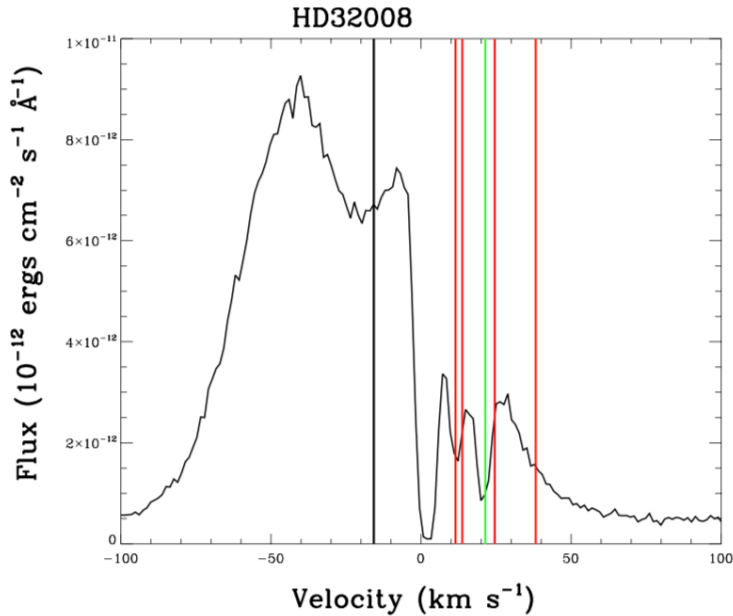


Figure 3.1: The radial velocity, plotted in black, aligns closely with the central reversal of the stellar emission line indicating this feature is stellar (this offset can be caused by radial velocity measurement discrepancies). The green and red lines represent the velocities of clouds the sightline is predicted to be passing through (green) and is nearby ($<20^\circ$).

Further considerations that help determine whether an extra-stellar feature is indicative of the ISM include that the radial velocities of ISM clouds are generally found between -25 km s^{-1} and $+25 \text{ km s}^{-1}$ (Redfield & Linsky 2002). Furthermore, because the ISM clouds are cold, the main broadening mechanism for ISM features is turbulent broadening. Turbulent broadening does not produce as dramatically broadened features as rotational broadening (common in stellar features) does (Malamut et al. 2014). Therefore, ISM absorption features are typically narrower than stellar features.

3.1.2 Fitting the Continuum

The fitting procedure itself begins with fitting a continuum to each spectrum. A continuum is created to mimic what the stellar target's spectrum would look like if it had no interstellar absorption. Any features that are characteristic of the ISM are skipped in the continuum fitting process (Figure 3.2). This continuum is referred to as the flux background. For most main sequence stars, there is a central reversal in the stellar ion emission features which aligns with the stellar radial velocity. Although at first glance the central reversal appears to be a possible ISM component, it is caused by a temperature inversion in the stellar atmosphere (Genova et al. 1990) and can be eliminated as a possible ISM absorption feature by its radial velocity.

The presence of ISM components near or within the central reversal of the stellar features complicates the creation of the flux background. Distinguishing the ISM features from the stellar features can be extremely challenging, particularly if vast portions of the stellar feature are convoluted by the ISM features (Figure 3.2).

The flux background itself is created using one of four methods: a polynomial fit, a user drawn continuum, flipping the profile, or sigma clipped fit. The polynomial fit is one of the more commonly used methods; it constructs a flux background through the user mandated process of selecting the region over which to skip (the ISM feature) and choosing the appropriate order of polynomial to fit the stellar continuum over the ISM absorption. The second fit method, user drawn continuum, allows the user to manually draw the flux background, and subsequently applies a smoothing function to better integrate the user-drawn portion into the entirety of the flux background. This method was used for particularly

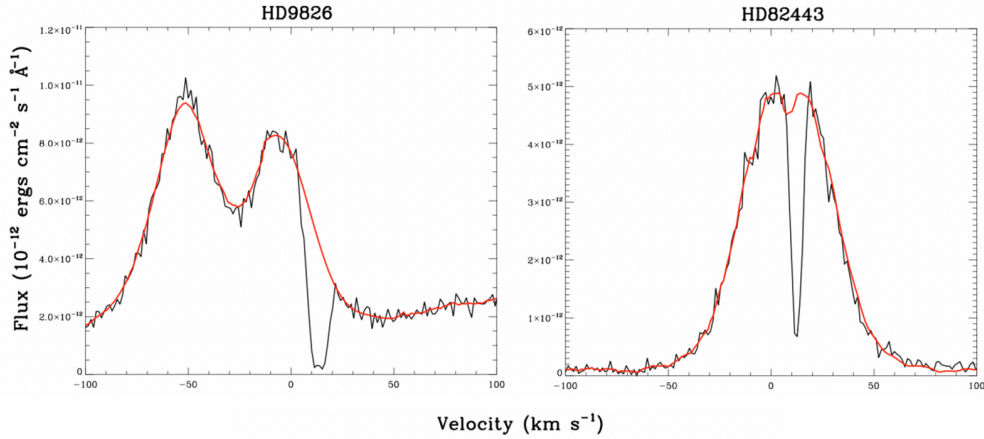


Figure 3.2: Examples of typical ISM absorption. HD9826’s spectrum shows a prominent ISM component whose radial velocity is significantly offset from the stellar radial velocity. HD82443’s spectrum shows an ISM absorption feature that occurs within the central reversal of the stellar emission. The slight offset in radial velocity and the depth of the feature indicate that this feature is interstellar. The red curve indicates the flux background.

low signal-to-noise spectra. Flipping the profile profile method works by mirroring the spectra itself over a specified axis (typically the radial velocity of the star), and then stitching the mirrored continuum with the original spectrum at the axis point so that the absorption feature is passed over. This method is particularly useful because the stellar emission features tend to be symmetric, so flipping the profile often ensures a realistic flux background. Finally, the sigma clipped fit method, the least used among the four, creates a flux background by iteratively discarding spectral data that does not fall within three sigma of the average flux value.

This flux background production process is completed separately for both the long and short emission wavelength of the ion doublet; these are then stitched together to form a flux background to be used in the simultaneous fit of the ISM absorption features. The signal of the continuum between the two emission lines

of the doublet is nearly zero, so even small variations between the continuum and the final fit can cause large errors that misleadingly increase the final χ^2 value. In order to minimize this effect on the systematic errors, the error arrays for the wavelengths between the two doublet wavelengths are made several orders of magnitude larger than the actual spectral data before they are used in the simultaneous fitting process.

3.1.3 Fitting the ISM Absorption

Once the stellar continuum has been established to bridge over the ISM absorption, the actual absorption fitting process begins. The procedure consists of fitting each absorption feature with as many Voigt profiles as statistically justifiable. Within a particular spectrum, multiple discrete ISM components can be present, so each are fit with an individual Voigt profile. A Voigt profile itself is a convolution of a Gaussian profile and a Lorentzian profile defined by its centroid, width, and depth. In some cases, like the spectrum in Figure 2.1, each discrete component can be easily identified. However in many cases, particularly for longer sightlines, individual components can become blended making it more difficult to identify individual clouds (Figure 3.3).

The three parameters of the Voigt profile – centroid, width, and depth – correspond to the physical cloud parameters of radial velocity, Doppler parameter (thermal and turbulent broadening), and column density respectively. In order to statistically determine the best fit to the data, our fitting program, combines the flux background of the spectrum with an input file containing various physical parameters such as initial guesses for the three absorption parameters, the wavelength range of absorption, and the line-spread function of the spectrograph

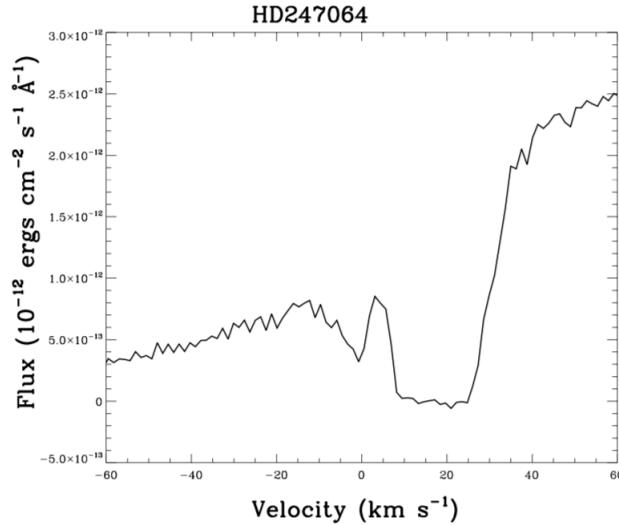


Figure 3.3: The spectrum of HD240764 indicates 2 discrete absorption features. However, the larger feature actually contains multiple blended components as indicated by its saturation and width. Final fits for this sightline indicate 4 discrete components with radial velocities at -1.44 ± 0.58 (NEW), 8.1 ± 2.68 (Hyades), 16.69 ± 0.50 (Aur), and 23.33 ± 1.00 (LIC).

itself. Using the values from the input file, a Marquart χ^2 minimization technique is used to fit the absorption features. This method works by varying the centroid wavelength, Doppler parameter, and column density around the initial guesses until a minimum value of χ^2 is reached. Once the program successfully runs and produces a fit, it executes a Markov chain Monte Carlo (MCMC) analysis to determine errors.

For each particular ion, the fitting procedure is independently performed three separate times: once for each line of the doublet and then a third time for the simultaneous fit. The simultaneous fit increases the constraints on the fit parameters by causing the features of the weaker absorption line to be linked to the stronger line. This fit serves to confirm the accuracy of the individual lines' fits and to increase the overall precision of the final fit parameters.

It is extremely common, particularly for longer sightlines, to detect the presence of multiple ISM features. Since ISM features typically have a radial velocity $\pm 25 \text{ km s}^{-1}$, for sightlines with multiple components, the individual ISM components often overlap and become blended (Figure 3.3). There are multiple methods for detecting and testing for the presence of individual components within blended features. The first indication that a seemingly single absorption feature actually contains multiple blended lines is its width. ISM features are typically narrow (having on average a Doppler parameter of 2.8 (Malamut et al. 2014)), so a particularly wide or saturated absorption feature is often an indication of multiple ISM components. Furthermore, the presence of multiple predicted clouds also motivates a multiple component fit.

For sightlines where it is unclear whether or not an additional ISM component should be present, after fitting is complete, a statistical test called the F-test is performed to determine if the additional ISM component is statistically probable. Due to the inevitable discrepancy between the Voigt model and the spectra themselves, adding additional absorption components added will often improve the overall fit (lower the χ^2). However, the presence of each additional component decreases the number of free parameters. The F-test statistically determines if the improvement of the fit is great enough to compensate for the loss of free parameters the additional component introduces. Figure 3.4 depicts an example of a sightline (HD17925) which passes the F-test for a three-component fit.

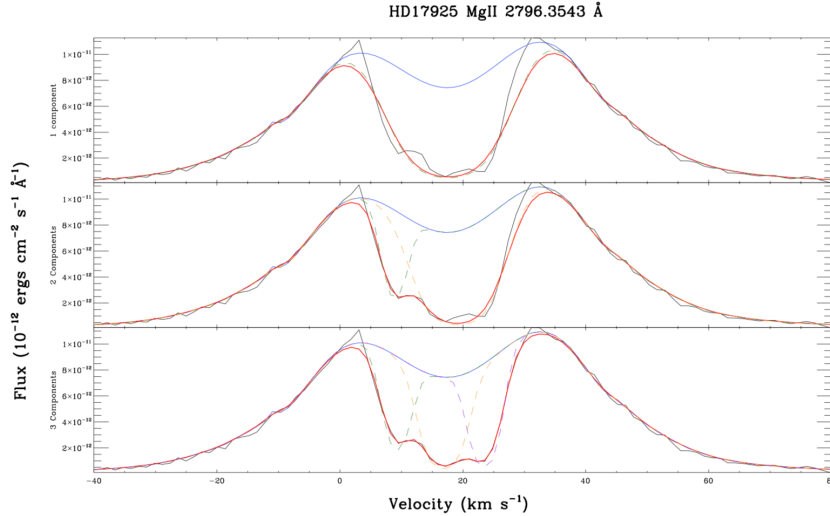


Figure 3.4: HD17925 has only two predicted ISM components within a particularly blended absorption feature. A high Doppler parameter ($b=6.12 \text{ km s}^{-1}$) and high χ^2 value for the 2 component fit prompted an attempt to fit the feature with three components. The fit with two components has a $\chi^2=7.69$ and 17 free parameters while the three-component fit has a $\chi^2=1.67$ and 14 free parameters; the F-test indicates that the two-component fit is statistically relevant and accurate.

3.1.4 Uncertainty and Error

For nearly every sightline in the survey, the systematic error dominates the random error. Some of the main sources of systematic error include the initial wavelength calibration of the spectrograph itself, the created flux background, the number of components, and observational aberrations. Although there always remains some level of error arising from observational uncertainties, the scattering of incoming light caused by the spectrograph's optics can be and has been precisely measured in order to be corrected for. This measurement produces a line-spread function that is applied to the data before the fitting procedure occurs in order

to ensure that the parameters of the absorption and emission features are true to the source. Despite this correction, many uncertainties in the data remain. Because there is no quantitative way to access the accuracy of the the created flux background, but the final fit is based so largely on it, the flux background remains a large contributor of the systematic error.

For each fit, the uncertainties for the 3 fit parameters are calculated using an MCMC error analysis. This process operates by putting random inputs into the model to estimate a probabilistic outcome. It is optimal for models whose systematic error dominates its random error, making it ideal for this particular survey. The overall error is calculated using the statistical analysis of reduced χ^2 .

In addition to convolving each spectrum with the line-spread function, there are several measures taken throughout the fitting process in an attempt to minimize errors and increase precision such as performing multiple independent fits per ion of a given sightline. Furthermore, since we base the accuracy of our fit off of its final χ^2 value, we take measures to ensure that only the emission line ranges are taken into account when calculating this value. As described in Section 3.1.2, the error values for the regions between the emission lines are artificially increased by multiple orders of magnitude to combat this region's misleading increase of the final χ^2 value.

Despite the efforts to minimize errors, there are often discrepancies between each fit of a given sightline. Because the flux background used for the fit depends so heavily on user input, there are always slight differences between the flux backgrounds for each emission wavelength. Additionally, the difference in emission strength and signal to noise of each of the emission lines themselves can result in differences in the final fit parameters for the same component. In order to combat this discrepancy, the final fit parameters and their uncertainties are

calculated through the process of taking a weighted mean of each of the ion's 3 fits. For blended and saturated features where these uncertainties become greater, additional measures such as the F-test (Section 3.1.3) are taken to ensure that the final fit has the highest statistic probability and the lowest possible uncertainty.

3.2 Fits

Out of the 37 sightlines, 3 were unable to be fit for MgII absorption due to 36 due to high stellar radial velocity offset (HD201091, HD33793, & HD13445). Out of the 34 remaining sightlines, the 2 most distant sightlines (HD188112 & BD+28D4211) exhibited extremely saturated and blended absorption features, so were only successfully fit in FeII at this time. In addition to these 2 distant sightlines, 3 others (HD160365, HD203244, & WD2211-495) were successfully fit in FeII, and 18 other sightlines show strong enough FeII emission to be fit in the future. The final fits for each sightline are presented in Figures 3.5 – 3.22, and the final fit parameters (radial velocity, Doppler parameter, and column density) are catalogued in Tables 3.1 & 3.2.

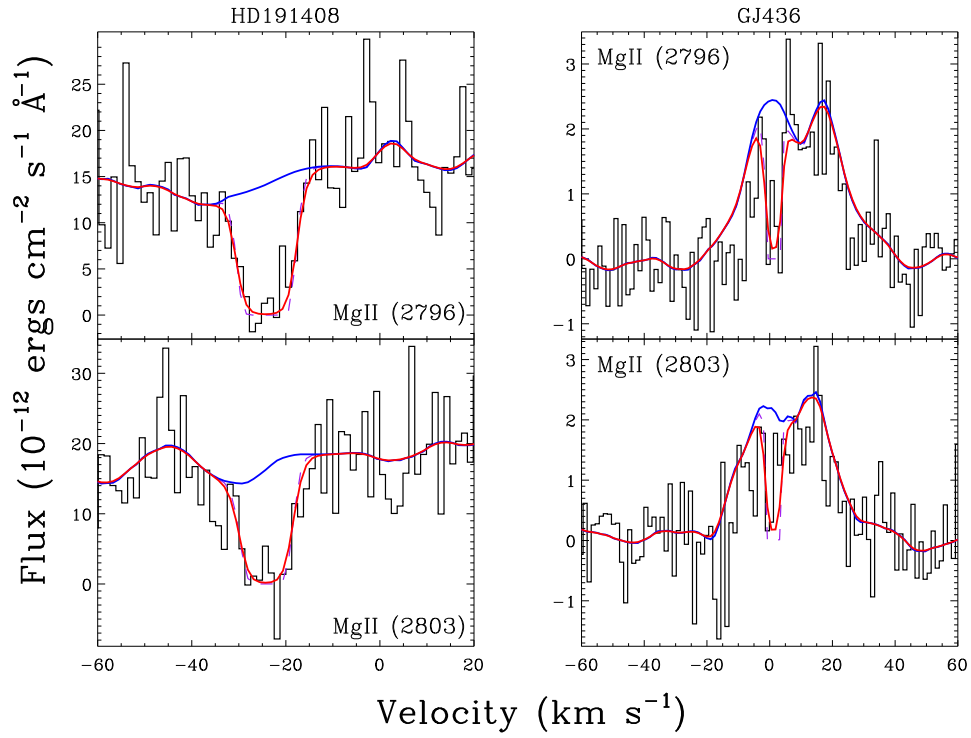


Figure 3.5: Simultaneous fits for MgII. The dashed lines are the individual component profiles (more noticeable for multiple component fits). The solid blue line is the continuum fit; the solid red line is the superposition of the individual components onto the continuum.

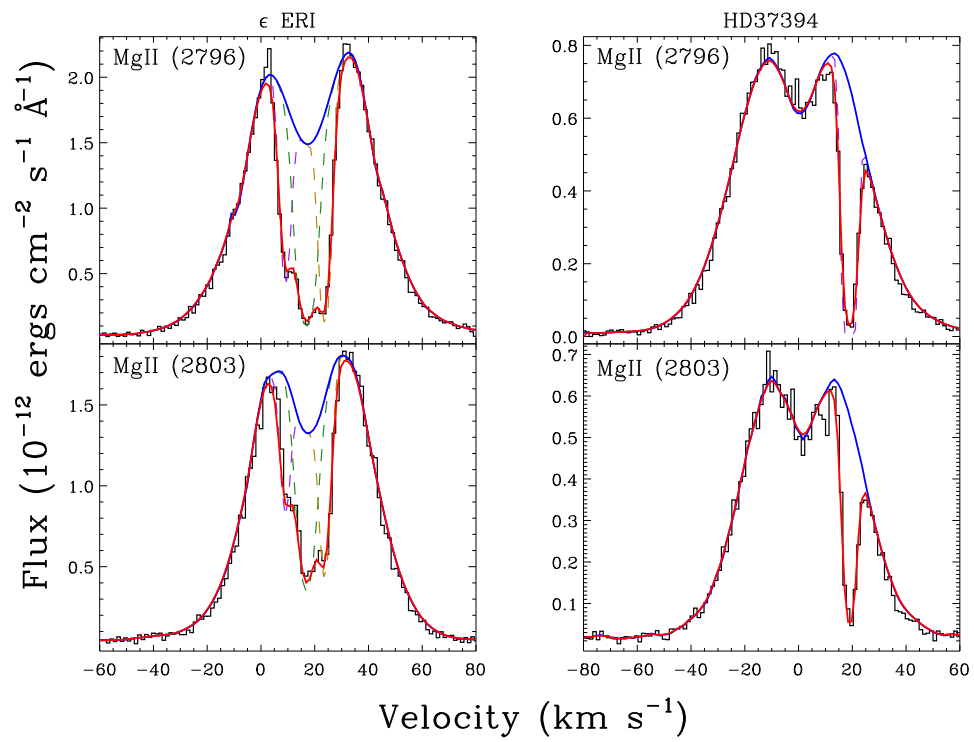


Figure 3.6: See caption of Figure 3.5.

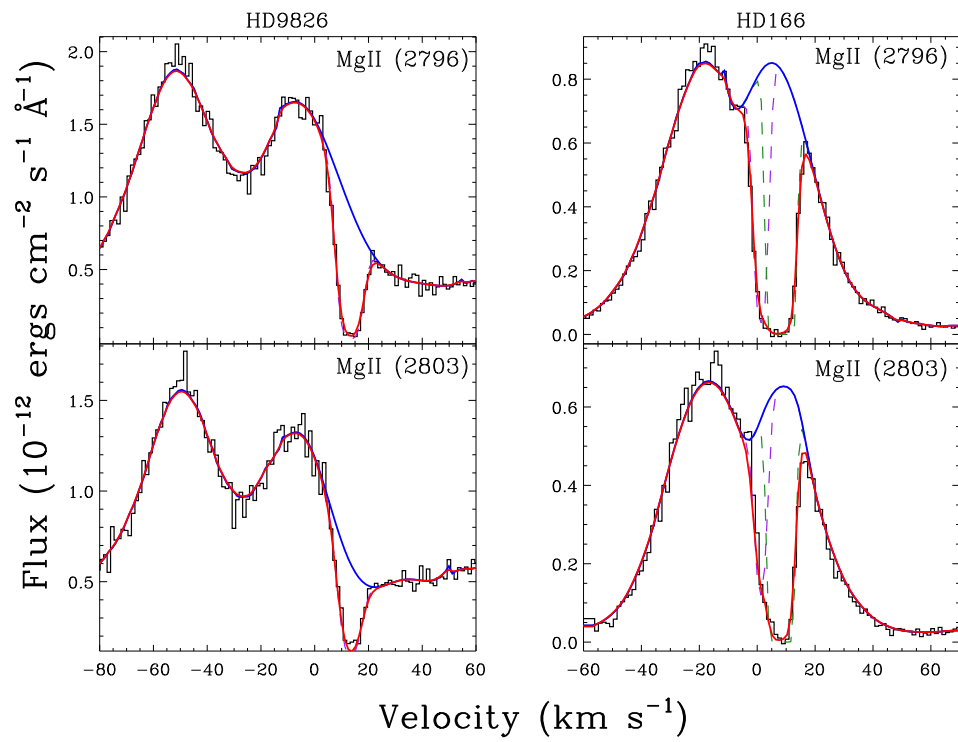


Figure 3.7: See caption of Figure 3.5.

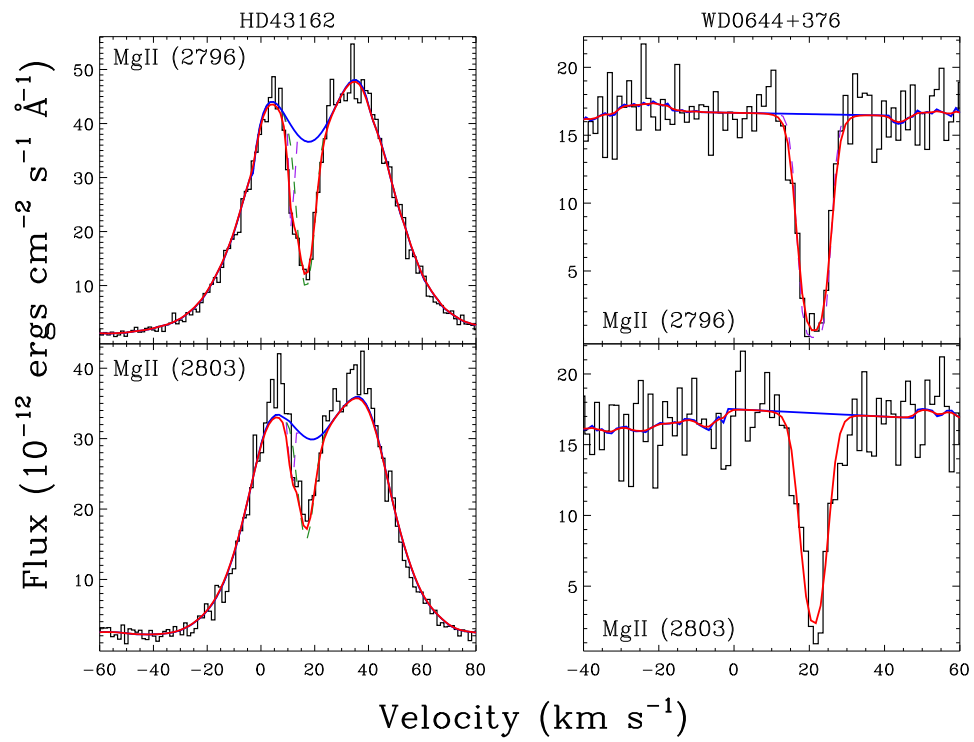


Figure 3.8: See caption of Figure 3.5.

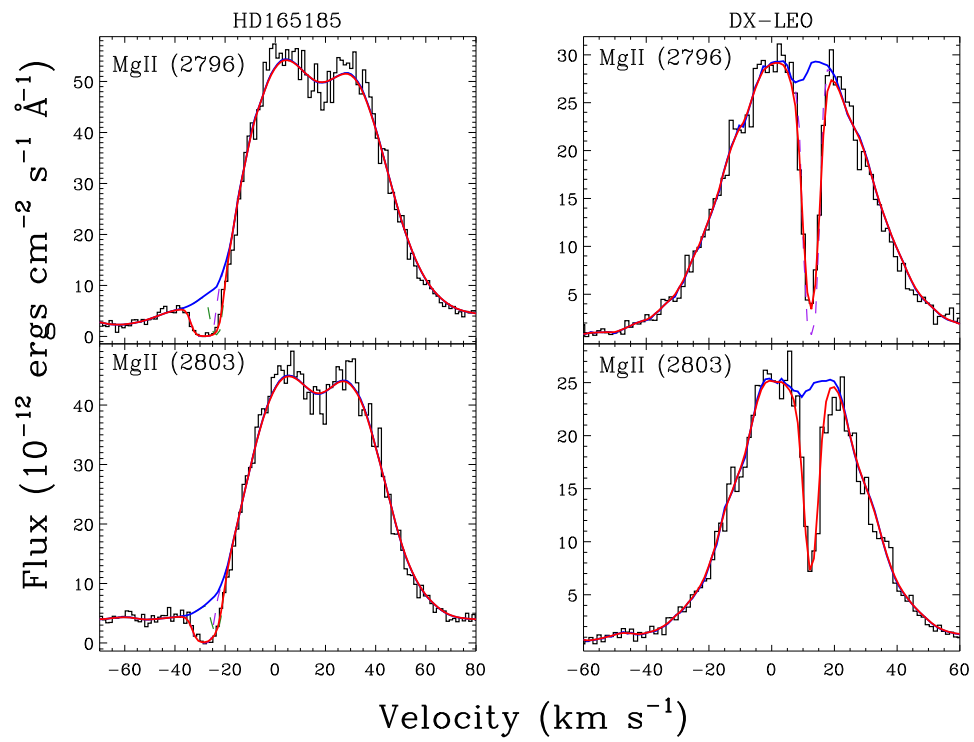


Figure 3.9: See caption of Figure 3.5.

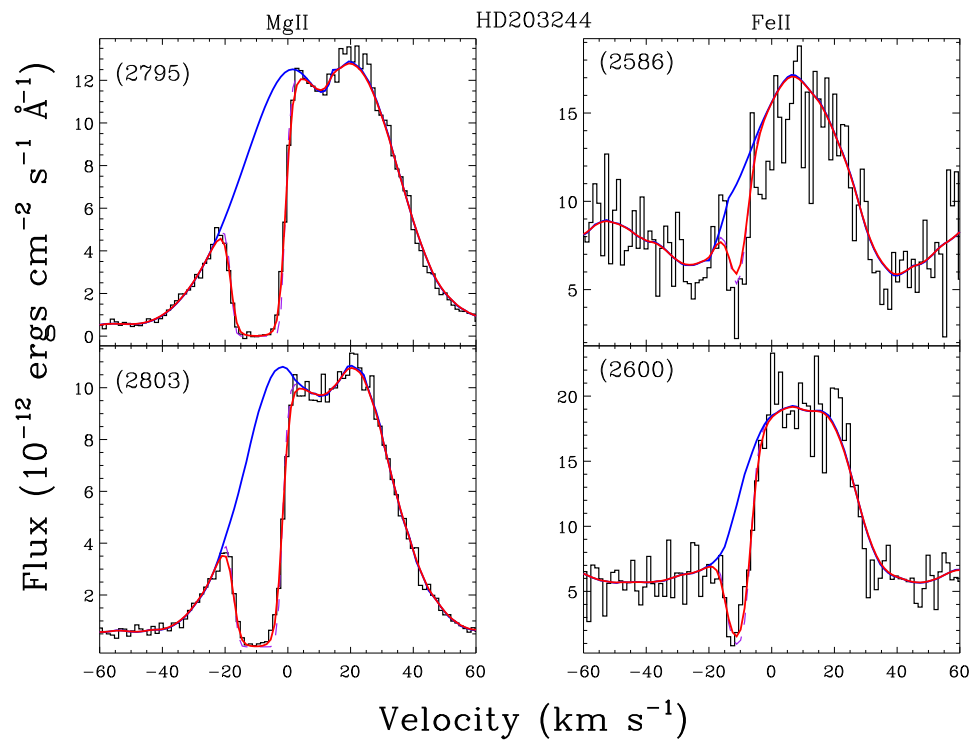


Figure 3.10: Simultaneous fits for both MgII and FeII. See caption of Figure 3.5

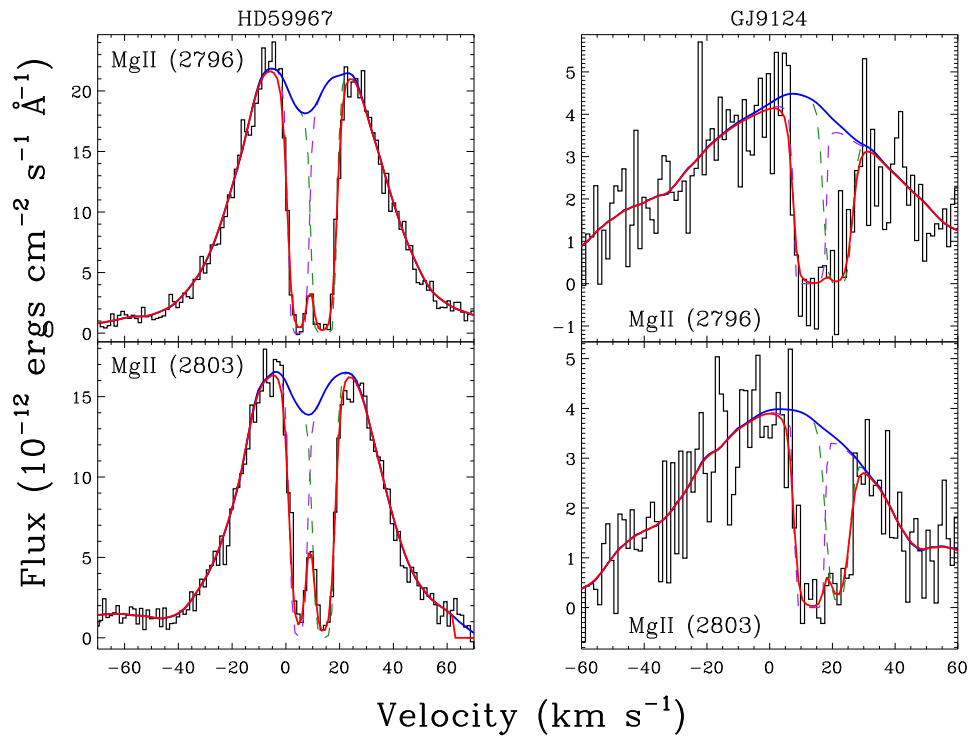


Figure 3.11: See caption of Figure 3.5.

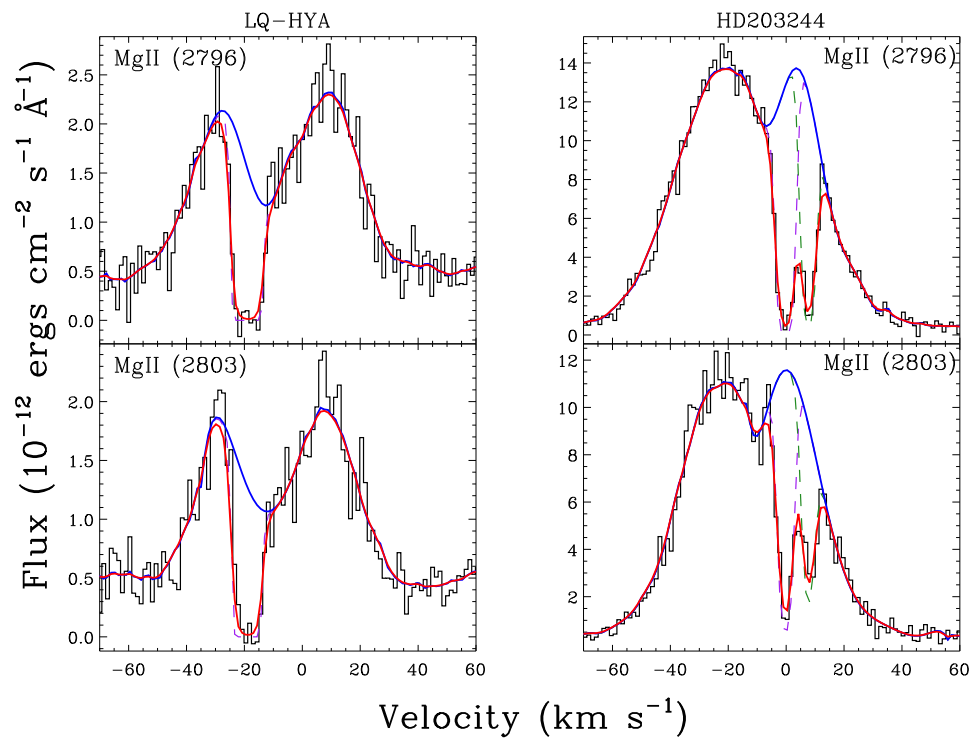


Figure 3.12: See caption of Figure 3.5.

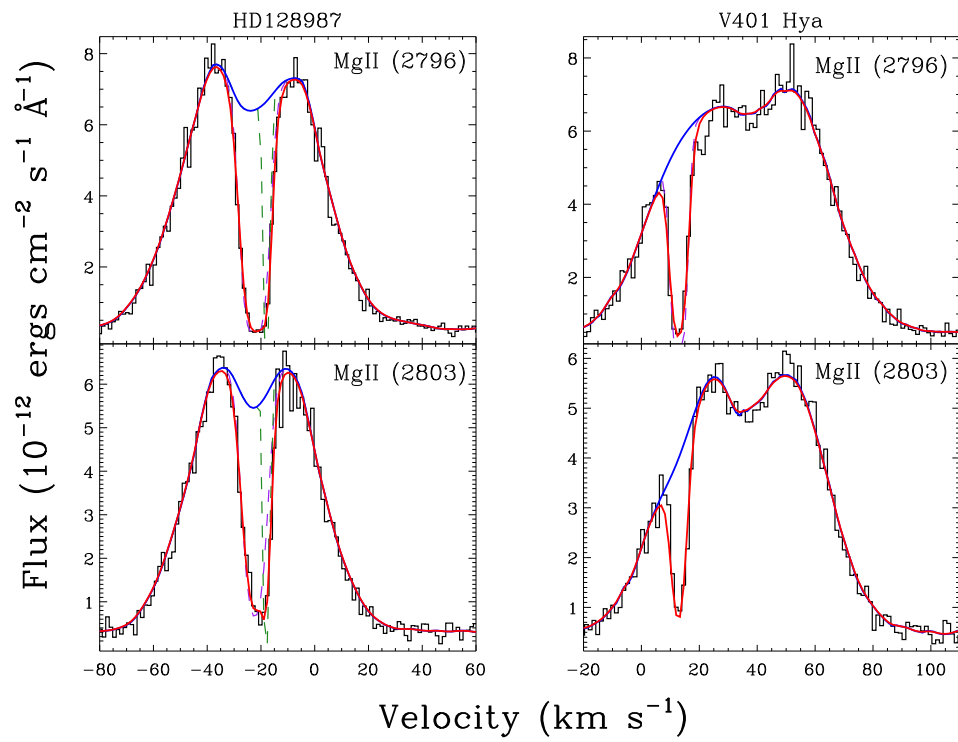


Figure 3.13: See caption of Figure 3.5.

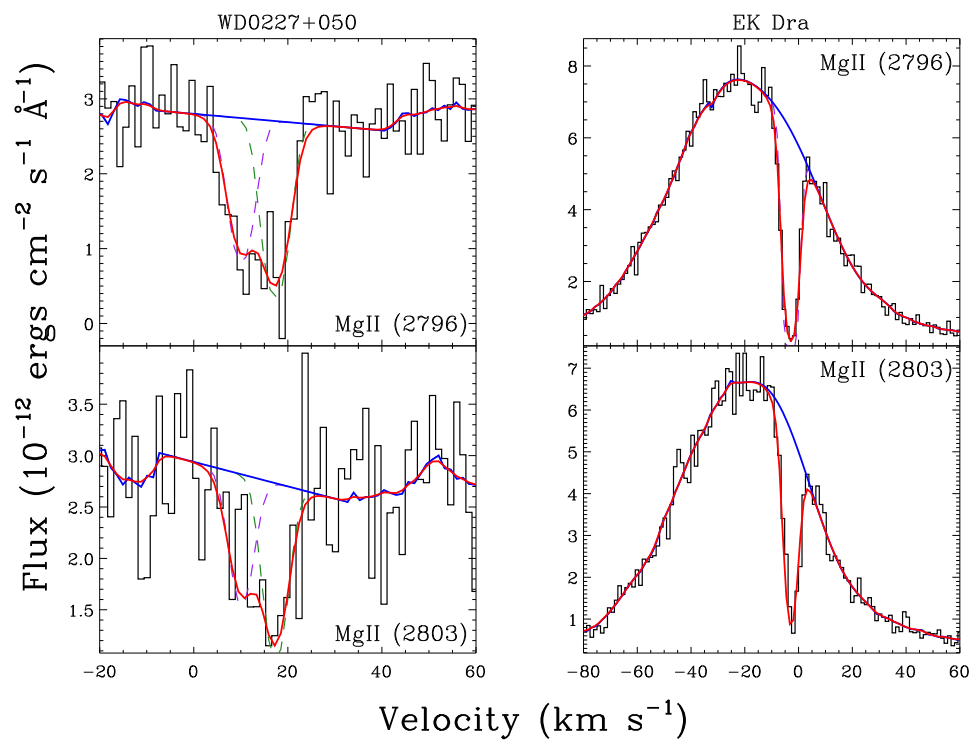


Figure 3.14: See caption of Figure 3.5.

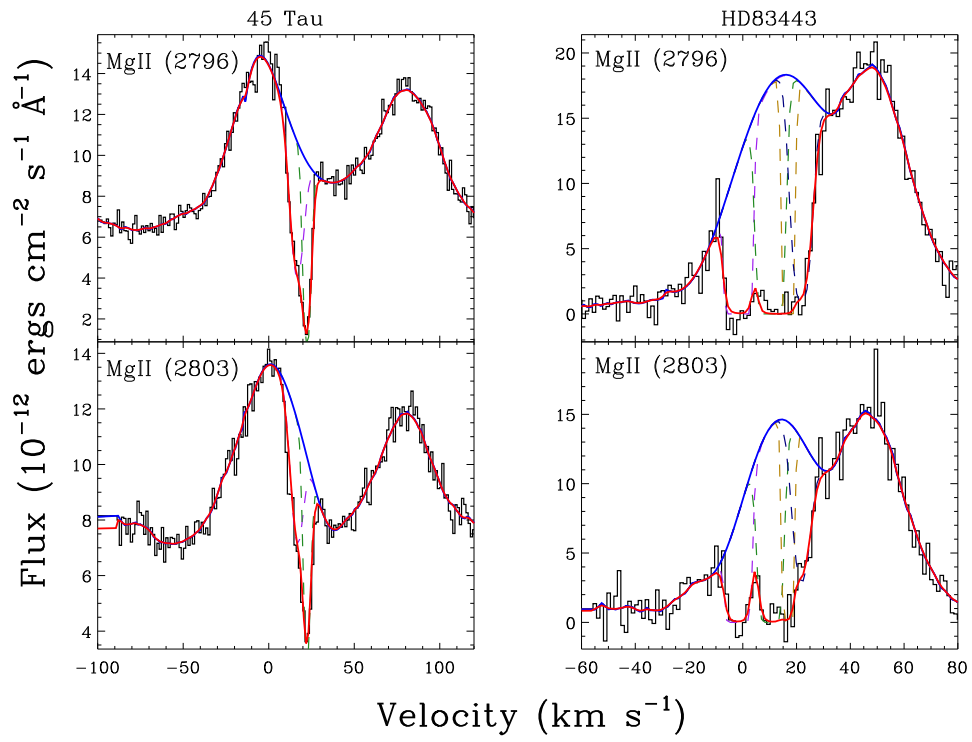


Figure 3.15: See caption of Figure 3.5.

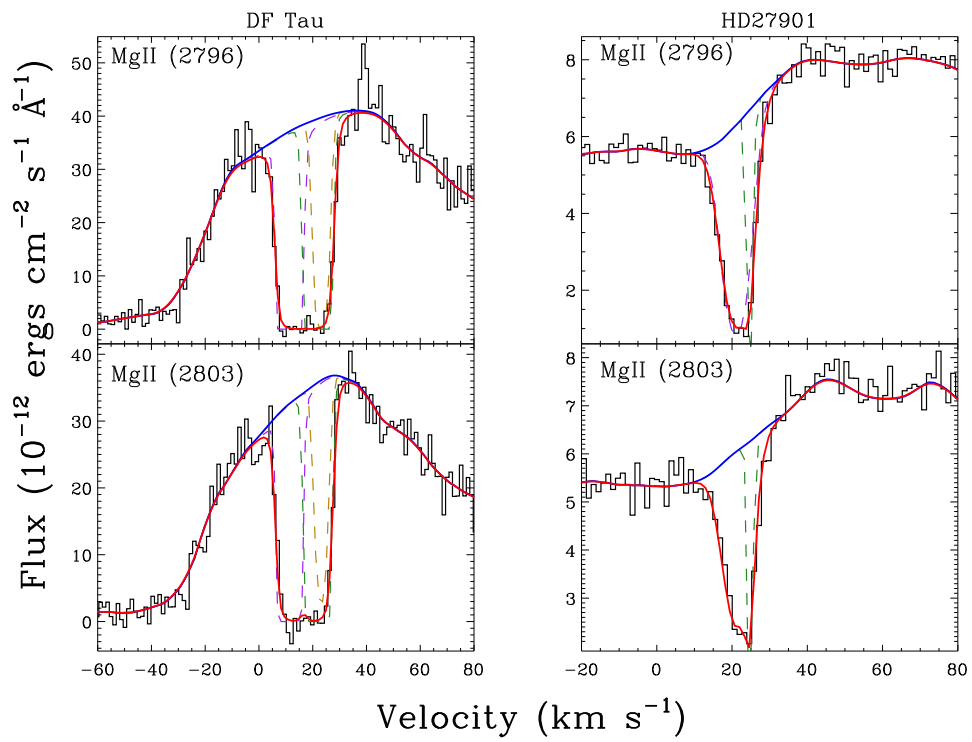


Figure 3.16: See caption of Figure 3.5.

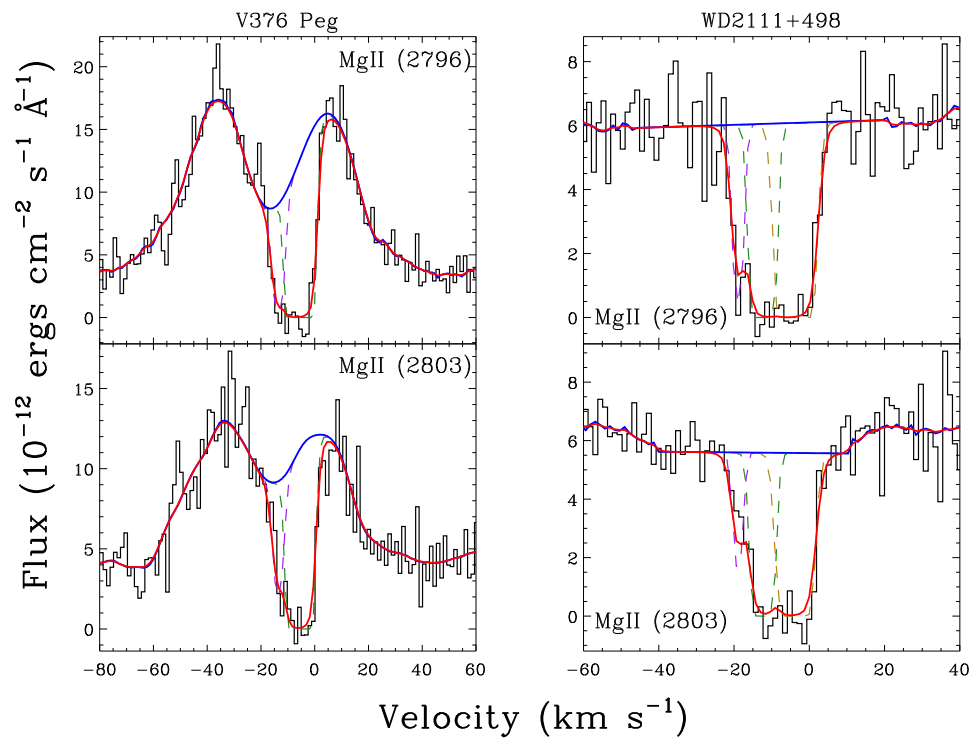


Figure 3.17: See caption of Figure 3.5.

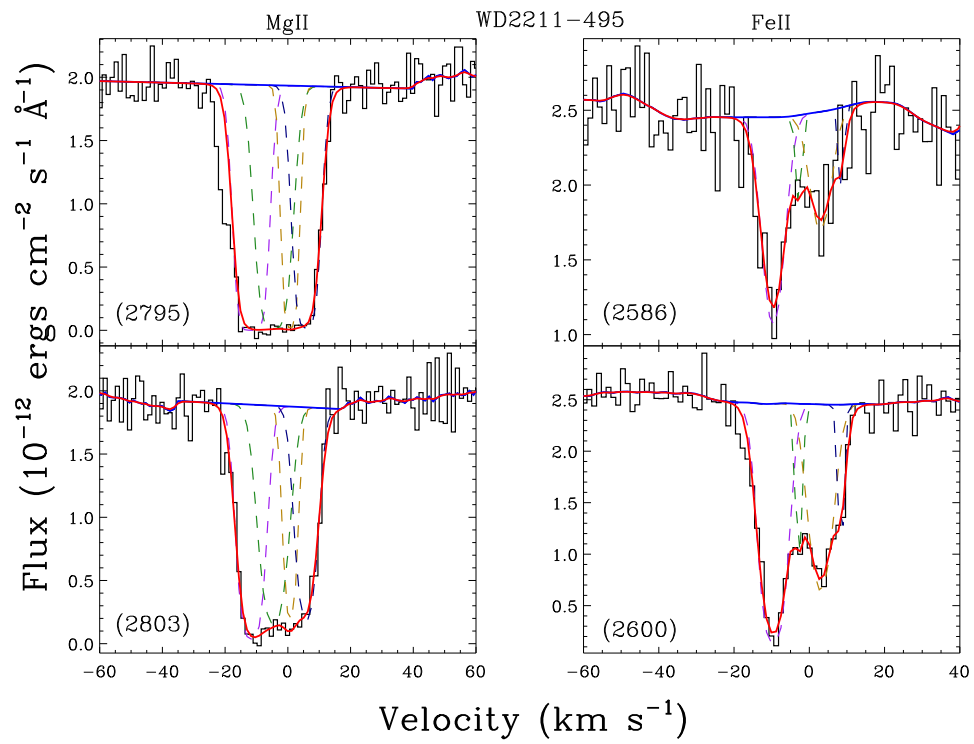


Figure 3.18: See caption of Figure 3.10.

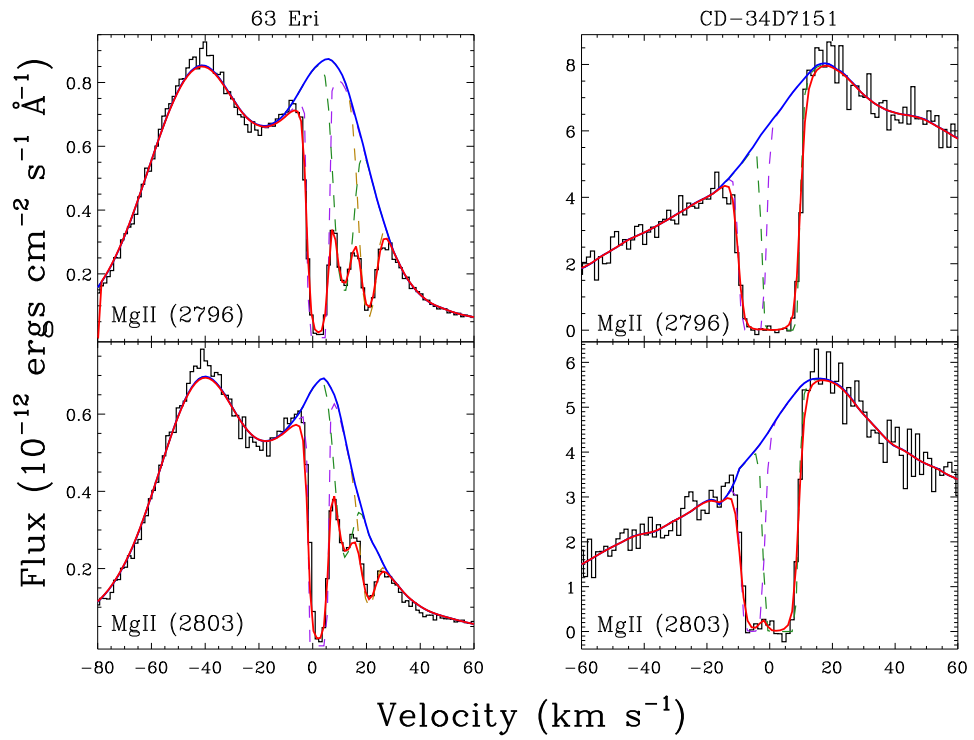


Figure 3.19: See caption of Figure 3.5.

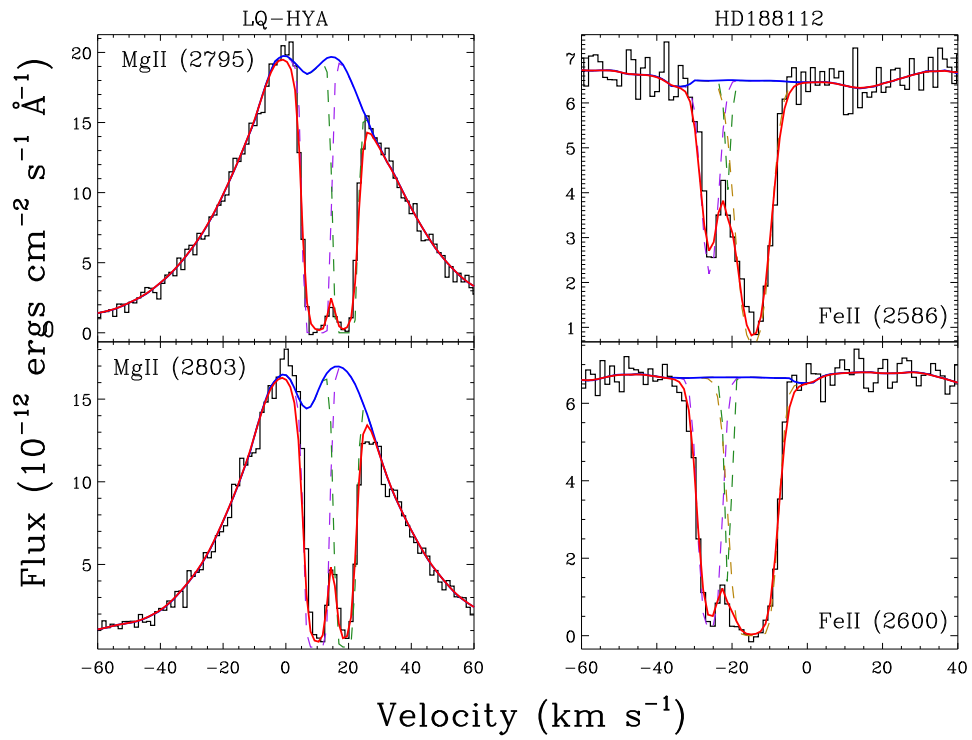


Figure 3.20: See caption of Figure 3.5.

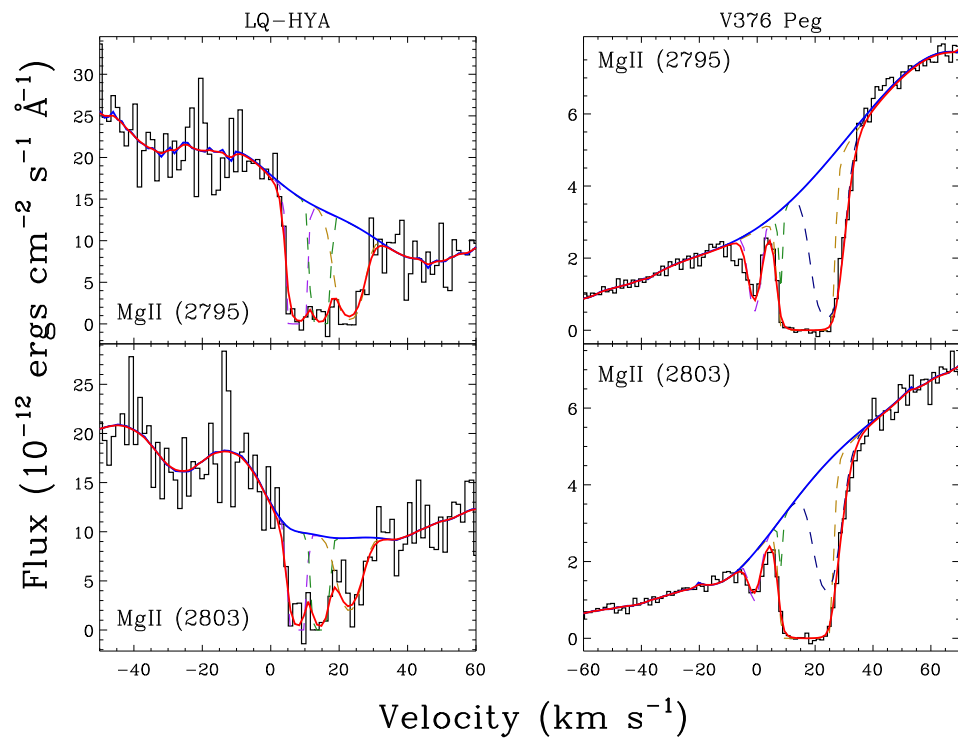


Figure 3.21: See caption of Figure 3.5.

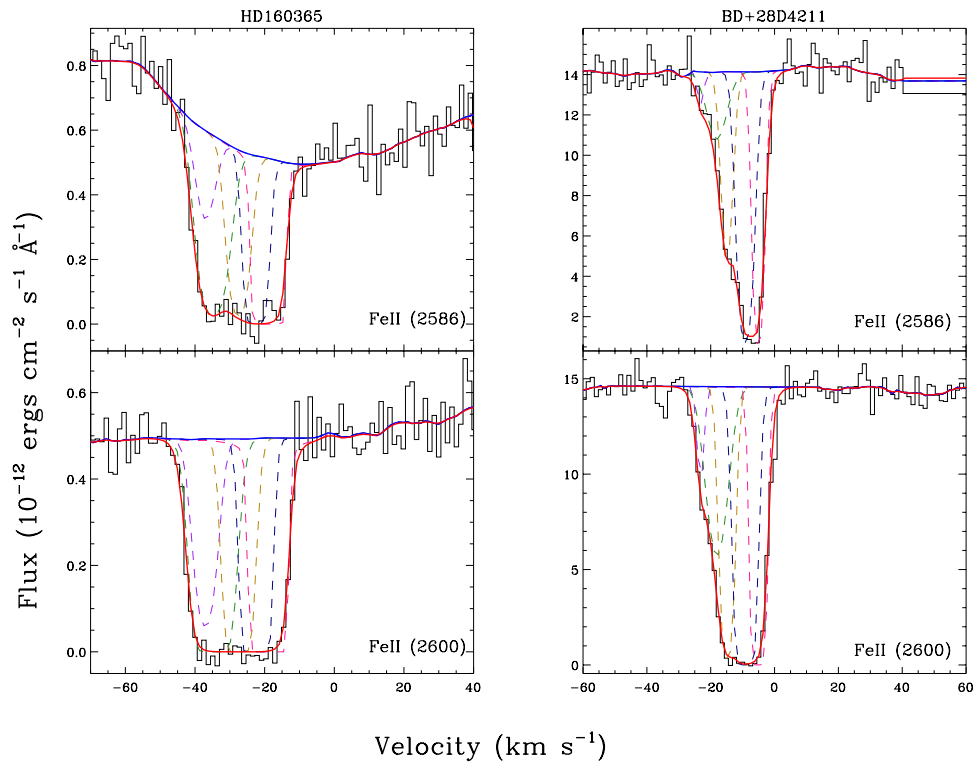


Figure 3.22: Simultaneous fits for FeII. See caption of Figure 3.5.

3.3 Final Fit Parameters

Final fits of each sightline are reviewed in four manners: through visual inspection for agreement between the data and final fit; through a consistency check of fit parameters for the sightline’s individual and simultaneous fits; through a comparison to the known distribution of the LISM; and finally, if necessary, through the F-test. Once a fit has passed all four reviews, the final fit parameters are calculated by taking a weighted mean of parameter values obtained from individual and simultaneous fits. In order to determine the plausibility of the fits with the distribution of LISM values, the final parameters are then compared to the predicted values of Redfield and Linsky’s LISM kinematic calculator (Redfield & Linsky 2008), and to the final parameters found in previous studies of the LISM (Malamut et al. 2014; Redfield & Linsky 2008).

The following tables (Tables 3.1 & 3.2) catalogue the final fit parameters for each sightline’s ISM components as obtained by the fitting procedure. The final fit parameters include the velocity (v), Doppler parameters (b), and log column densities ($\log N$). For those sightlines that did not have a high enough signal-to-noise ratio for FeII emission to be independently fit, an upper limit on column density can instead be calculated (see Section 3.3.1). Although HD188112 and BD+28D42411 also exhibit significant MgII absorption, due to severe blending and saturation their spectra were unable to reliably be fit at this time, so their final MgII fit parameters are not listed; they do have final fit parameters listed for FeII.

3.3.1 Upper Limits

MgII, being a lighter element than FeII, has a stronger emission line. Because of this, for many sightlines, MgII emission was detected, but the signal-to-noise ratio for the FeII emission was too low for definitive emission/absorption features to be detected. When this is the case, an upper limit on the column density of a cloud can be calculated. Based on the assumption that the LISM clouds are well mixed, the upper limit on the column density for the FeII ion should be well correlated to the measured column density from the MgII emission.

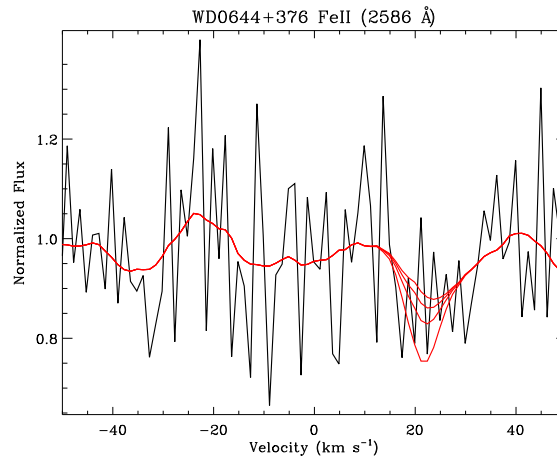


Figure 3.23: As indicated by the fit of MgII, WD0644+376’s sightline traverses 1 cloud (LIC: $v_r = 21.29 \pm 0.31 \text{ km s}^{-1}$). However, due to low signal to noise, this feature is not detectable in the spectrum’s FeII emission. The dotted lines represent absorption features at various column densities, the deepest of which ($\log N = 12.4$) is the upper limit for this particular feature.

The process of calculating an upper limit consists of creating a series of Voigt profiles with varying column densities and calculating the area each profile produces under a normalized spectra. The upper limit for the column density is chosen as the largest value whose corresponding area does not exceed three times the root mean square (RMS) of the normalized data. The upper limit is chosen

as the largest absorption profile that does not exceed three times the RMS (the 3σ upper limit). Figure 3.23 shows an example of the process of calculating the upper limit of ISM absorption in the FeII emission of WD0644+376.

Table 3.1: MgII Fit Parameters for Survey

HD No.	Other Name	Component No.	v (km s ⁻¹)	b (km s ⁻¹)	$\log N_{MgII}$ log(cm ⁻²)
191408	HIP99461	1	-24.35 ± 0.50	3.82 ± 0.62	13.16 ± 0.43
	GJ436	1	1.52 ± 4.3	1.08 ± 0.62	13.63 ± 0.74
17925	ϵ -ERI	1	9.23 ± 0.24	2.46 ± 0.33	12.15 ± 0.03
		2	17.06 ± 0.41	3.91 ± 0.55	12.62 ± 0.03
		3	23.94 ± 0.49	2.43 ± 0.29	12.39 ± 0.04
37394	HIP26779	1	18.95 ± 0.17	12.19 ± 0.08	12.89 ± 0.05
9826	ν -AND	1	13.22 ± 0.06	4.18 ± 0.09	12.79 ± 0.01
166	HR8	1	2.60 ± 1.06	2.77 ± 0.63	12.59 ± 0.09
		2	8.85 ± 0.55	2.69 ± 0.38	13.64 ± 0.21
43162	HD43162	1	11.57 ± 0.40	1.17 ± 0.47	11.57 ± 0.14
		2	16.85 ± 0.24	3.47 ± 0.29	12.27 ± 0.03
	WD0644+376	1	21.29 ± 0.31	3.38 ± 0.30	12.83 ± 0.04
165185	HD165185	1	-28.55 ± 1.09	2.73 ± 0.45	13.1 ± 0.26
		2	-23.47 ± 2.72	2.66 ± 0.49	12.24 ± 0.20
82443	HD82443	1	12.56 ± 0.26	2.22 ± 0.09	12.48 ± 0.03
82558	HD82558	1	9.98 ± 0.51	2.18 ± 0.20	13.59 ± 0.24
		2	18.91 ± 0.36	2.36 ± 0.13	13.18 ± 0.07
203244	HD203244	1	-9.59 ± 0.19	4.43 ± 0.07	13.80 ± 0.04
199288	HD199288	1	-19.00 ± 0.39	2.53 ± 0.30	14.03 ± 0.35
116956	HD116956	1	-0.15 ± 0.08	-2.53 ± 0.15	12.81 ± 0.05
		2	7.72 ± 0.10	2.35 ± 0.37	12.51 ± 0.03
59967	HD59967	1	4.79 ± 0.39	2.51 ± 0.46	12.89 ± 0.10
	GJ9124	1	13.03 ± 0.78	1.9 ± 0.32	14.74 ± 0.37
		2	21.94 ± 0.67	2.84 ± 0.69	12.95 ± 0.30
128987	HD128987	1	-22.30 ± 0.51	-4.37 ± 0.22	12.85 ± 0.04
		2	-17.94 ± 0.57	1.06 ± 0.85	12.74 ± 0.35
	CD-34D7151	1	-5.49 ± 0.28	2.48 ± 0.66	13.18 ± 0.19
		2	3.53 ± 0.22	2.71 ± 0.20	14.03 ± 0.21
73350	HD73350	1	12.92 ± 0.26	2.43 ± 0.1	12.66 ± 0.03
	WD0227+050	1	10.32 ± 0.91	3.33 ± 1.17	12.14 ± 0.11
		2	17.55 ± 0.90	2.58 ± 1.13	12.41 ± 0.08
129333	HD129333	1	-2.6 ± 0.35	2.546 ± 0.11	12.71 ± 0.03
26462	HD26462	1	15.76 ± 0.51	4.19 ± 0.41	12.15 ± 0.01
		2	22.00 ± 0.22	2.54 ± 0.40	12.42 ± 0.01
83443	HD283654	1	-1.59 ± 0.32	2.45 ± 0.41	14.07 ± 0.39
		2	9.82 ± 0.94	3.2 ± 0.98	13.15 ± 0.38
		3	16.66 ± 0.74	2.76 ± 0.86	13.62 ± 0.37
		4	22.41 ± 0.90	3.41 ± 0.91	12.46 ± 0.16
283654	HD283654	1	11.70 ± 0.40	3.53 ± 0.79	13.36 ± 0.18
		2	21.6 ± 0.40	2.6 ± 0.45	13.96 ± 0.39
		3	23.43 ± 0.68	2.67 ± 0.49	12.72 ± 0.47
27901	HD27901	1	21.19 ± 0.50	4.26 ± 0.16	12.52 ± 0.02
		2	24.73 ± 0.42	0.71 ± 0.20	12.04 ± 0.15
209458	HD209458	1	-12.39 ± 1.23	2.39 ± 0.79	12.44 ± 0.32
		2	-5.07 ± 0.74	2.58 ± 0.59	13.71 ± 0.49
	WD2111+498	1	-18.93 ± 0.41	1.46 ± 0.48	12.14 ± 0.10
		2	-11.84 ± 0.78	2.55 ± 0.64	13.61 ± 0.20
		3	-3.43 ± 0.94	2.55 ± 0.96	13.34 ± 0.28
32008	HD32008	1	2.02 ± 0.21	1.65 ± 0.42	13.50 ± 0.15
		2	11.57 ± 0.11	3.87 ± 0.13	12.42 ± 0.01
		3	20.69 ± 0.17	3.13 ± 0.22	12.41 ± 0.01
	WD2211-495	1	-11.47 ± 0.52	4.02 ± 0.57	13.15 ± 0.07
		2	-4.36 ± 0.52	-4.96 ± 1.22	12.88 ± 0.20
		3	0.97 ± 0.52	1.62 ± 0.61	12.74 ± 0.13
		4	6.07 ± 0.52	3.6 ± 0.48	12.81 ± 0.07
240764	RW Aur	1	-1.44 ± 0.58	3.72 ± 0.71	12.18 ± 0.01
		2	8.1 ± 2.68	0.79 ± 0.85	12.08 ± 0.13
		3	16.69 ± 0.50	3.67 ± 0.33	14.70 ± 0.11
		4	23.33 ± 1.00	5.39 ± 0.52	12.83 ± 0.02
33959C	HD33959C	1	7.72 ± 0.49	1.71 ± 0.28	12.79 ± 0.53
		2	14.73 ± 0.74	1.99 ± 0.51	13.11 ± 0.36
		3	23.46 ± 0.86	3.55 ± 0.83	12.68 ± 0.09

Table 3.2: FeII Fit Parameters for Survey

HD No.	Other Name	Component No.	v (km s ⁻¹)	b (km s ⁻¹)	$\log N_{MgII}$ log(cm ⁻²)
203244	HIP105712	1	-10.88 ± 0.30	3.6 ± 0.83	12.97 ± 0.05
		2	-9.52 ± 0.25	3.62 ± 0.27	13.09 ± 0.06
	WD2211-495	1	-2.26 ± 0.67	3.17 ± 1.24	12.13 ± 0.14
		3	13.06 ± 0.25	13.06 ± 0.55	12.65 ± 0.04
HD188112	HIP97962	4	8.32 ± 0.74	1.42 ± 0.51	12.07 ± 0.14
		1	-25.73 ± 0.23	2.42 ± 0.43	13.02 ± 0.03
		2	-20.23 ± 0.73	1.29 ± 0.74	12.32 ± 0.14
		3	-13.73 ± 0.52	3.94 ± 0.28	13.52 ± 0.05
160365	HIP86373	1	-37.02 ± 1.14	3.60 ± 2.23	12.98 ± 0.24
		2	-34.84 ± 1.14	4.24 ± 2.77	13.02 ± 0.23
		3	-27.48 ± 1.16	5.86 ± 2.88	12.92 ± 0.09
		4	-22.47 ± 1.17	2.41 ± 3.2	13.95 ± 0.32
		5	-18.96 ± 1.18	2.23 ± 0.63	14.53 ± 0.16
	BD+28D4211	1	-22.42 ± 0.52	1.8 ± 0.52	12.01 ± 0.09
		2	-15.93 ± 1.46	3.743 ± 0.8	12.78 ± 0.04
		3	-13.26 ± 0.93	2.74 ± 0.51	13.02 ± 0.06
		4	-9.31 ± 0.49	2.00 ± 0.91	13.15 ± 0.04
		5	-5.69 ± 0.57	1.76 ± 0.19	13.32 ± 0.07

Chapter 4

Results and Analysis of Sample

The analysis of the 37 sightlines in the sample returned a set of final fit parameters that characterize the velocity, column density, and Doppler parameter of 76 discrete LISM clouds. Between the 34 sightlines successfully fit in this survey, 62 individual components were identified in MgII and 19 were identified in FeII. Due to low signal to noise and high radial velocity offset, 3 sightlines (HD201091, HD33793, & HD13445) were unable to be fit for either ion. Many of the sightlines in this survey do exhibit strong enough emission to be fit in FeII, however, due to the time constraint, their final fits cannot be showed at this time. Additionally, the survey's 2 longest sightlines (HD160365 and BD+28D4211) show strong enough emission in MnII (2594.499 Å and 2606.462 Å) for its absorption features to be fit in the future as well. Table 4.1 presents the average values and standard deviation for the Doppler parameter and column density the fits. Figures 4.1, 4.2, & 4.3 show the distribution of each of the final fit parameters across all of the fitted sightlines for each ion.

Table 4.1: Mean Values for Doppler Parameter and Log Column Density

Ion	No. of fits	$\langle b \rangle$ (km s ⁻¹)	σ_b (km s ⁻¹)	$\langle \log N \rangle$ log(cm ⁻²)	$\sigma_{\log N}$ log(cm ⁻²)
MgII	62	2.90	1.06	12.94	0.65
FeII	19	2.74	1.29	12.91	0.66

4.1 The Velocity Distribution

The velocities of individual components in this sample range from -37.02 to 24.73 km s^{-1} . Although individual clouds do have distinct motions, they tend to move together with similar direction and velocity (Frisch et al. 2002; Redfield & Linsky 2008) causing the relatively small range of velocity values. Figure 4.1 shows the distribution of all identified components' velocities for both of the ions.

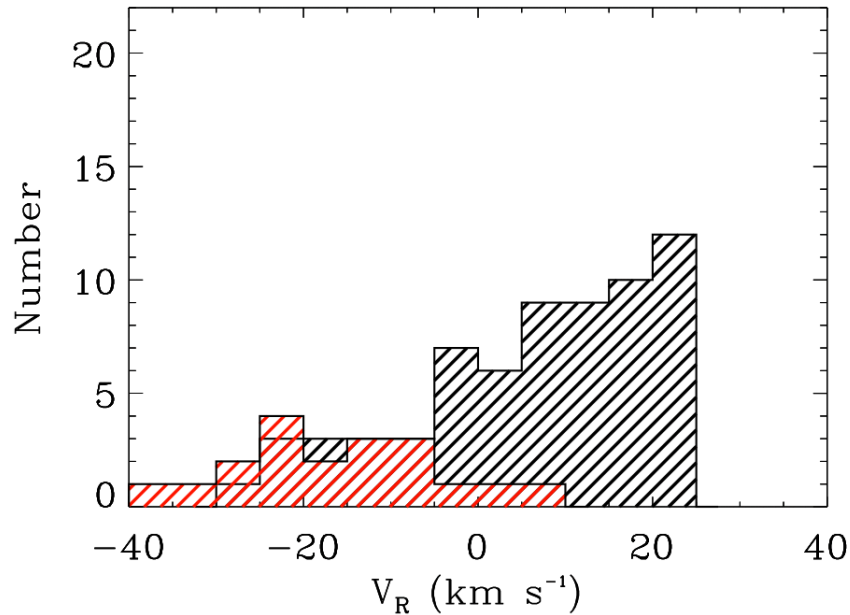


Figure 4.1: Distribution for the radial velocities for observed ions in the survey. Black represents the MgII distribution (62 components) while red is the FeII distribution (19 components). The bin size of the distribution is 5 km s^{-1} .

Since the components measured across multiple ions of one particular spectrum represent the same LISM clouds, we expect the distribution of radial velocity to be similar for FeII and MgII. The discrepancy in this distribution, values for FeII appearing to be skewed to more negative values, this is a result of the selection bias of the successfully fitted sightlines. The majority of sightlines which have been

successfully fit for FeII absorption at this time are the longer sightlines (>60 pc) of the survey. Because of this, they are traversing many clouds not measured by the shorter sightlines, and therefore not present in the MgII distribution. Additionally, the velocity of the components from the 2 longest sightlines are only included in the FeII distribution because they have not yet been successfully fit in MgII; this adds to the apparent discrepancy between the distributions.

Despite the fact that the distributions of velocities for each ion cannot be usefully compared to each other at this time, the overall distribution shape and density are consistent with the findings of previous surveys. Malamut et al. 2014 found a range of component velocities -32 to $+25$ km s $^{-1}$ and Redfield & Linsky 2004 found a velocity range of -43 to $+33$ km s $^{-1}$. Additionally, the velocity distribution is consistent with the bulk velocity of the warm LISM clouds: 28.1 ± 4.6 km s $^{-1}$ (Frisch et al. 2011). Furthermore, the distribution range does confirm the findings of Redfield & Linsky (2002) that the radial velocities of ISM clouds are generally found between ± 25 km s $^{-1}$. 95% of the velocities measured in this survey fall within this range.

4.2 The Doppler Parameter Distribution

The Doppler parameter (b) is a measure of the broadening of an absorption feature and is related to the temperature and turbulence of a given cloud following the equation:

$$b^2 = \frac{2kt}{m} + \xi^2 = 0.016629 \frac{T}{A} + \xi^2,$$

where T is the cloud's temperature, ξ is the cloud's turbulent velocity, A is the ion's atomic weight, m is the ion's mass, and k is the Boltzmann constant. Tur-

bulence is the dominant mechanism for absorption line broadening for heavy elements, but thermal broadening plays a significant role in increasing the Doppler parameter for lighter ions. Because of this, the Doppler parameters from the lighter ion's, MgII, fits tend to be larger than the corresponding values from the FeII fits. Figure 4.2 shows the distribution of b values for the survey; the values range from 0.71 to 5.86 km s⁻¹.

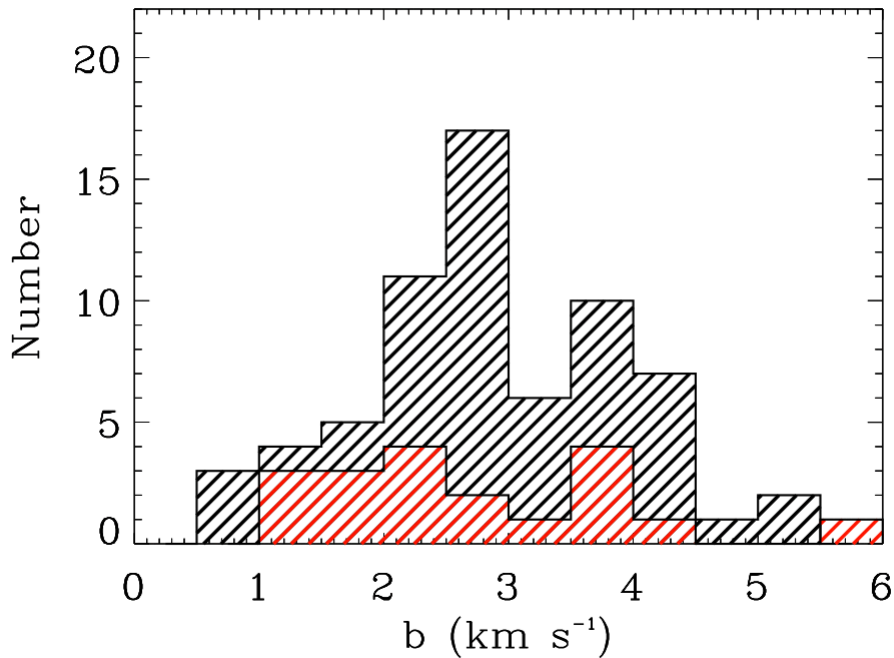


Figure 4.2: Distribution for the Doppler parameter (b) for observed ions in the survey. Black represents the MgII distribution (62 components) while red is the FeII distribution (19 components). The bin sizes of the distribution are 0.5 km s⁻¹.

While again, due to the selection bias, it is difficult to meaningfully compare the distributions from the two ions to each other. However, we do see a larger percentage of the FeII distribution with b values less than 2.90 km s⁻¹, the average of the MgII values. 63% of the FeII b values fall below the 2.90 km s⁻¹ average of

the MgII values. Additionally, the average b values for each ion are consistent with those measured in previous surveys: Redfield & Linsky (2002) reported values of $\langle b(FeII) \rangle \sim 2.4 \text{ km s}^{-1}$ and $\langle b(MgII) \rangle \sim 3.1 \text{ km s}^{-1}$, while Malamut et al. (2014) reported values of $\langle b(FeII) \rangle \sim 2.72 \text{ km s}^{-1}$ and $\langle b(MgII) \rangle \sim 3.36 \text{ km s}^{-1}$. Although my $\langle b(MgII) \rangle$ value is slightly below both of the previously reported values, my $\langle b(FeII) \rangle$ is extremely consistent with the findings of Malamut et al. (2014) and my distribution range for both ions is consistent with both of the previous surveys.

4.3 The Column Density Distribution

Figure 4.3 shows the distribution of column densities of the survey. The parameter presented is the \log_{10} of the column density (N) of the particular ion, and the values range from 11.57 to 14.74 $\log(\text{cm}^{-3})$ with a mean value of 12.94 $\log(\text{cm}^{-3})$ for MgII and 12.91 $\log(\text{cm}^{-3})$ for FeII. While these values are slightly larger than the mean values reported by Redfield & Linsky (2002): $\langle \log N_{MgII} \rangle = \langle \log N_{FeII} \rangle = 12.45 \log(\text{cm}^{-3})$, they do exhibit a similar self consistency and are similar to the mean values reported in Malamut et al. (2014): $\langle \log N_{MgII} \rangle = 12.89 \log(\text{cm}^{-3})$ and $\langle \log N_{FeII} \rangle = 12.61 \log(\text{cm}^{-3})$.

The column density is a two-dimensional density measurement for a particular ion along the sightline assuming a cylinder whose length is the length of the sightline and whose cross-sectional area is 1 cm^2 . It is a measurement determined from the gas phase abundance of the ion. Despite the fact that Mg and Fe do not have the highest elemental gas phase abundances in the ISM (due to depletion onto interstellar dust grains), we choose to analyze MgII and FeII because these are the dominant ionization stages of these two elements. This results in their particularly

high emission strength (Slavin & Frisch 2008) leading to more direct and accurate measurements of the column density. Despite the differences in length and component number of the sightlines represented in the MgII distribution compared to the FeII distribution, the distributions are fairly consistent. This consistency can most likely be attributed to the similarities of MgII and FeII’s abundances and ionization strengths.

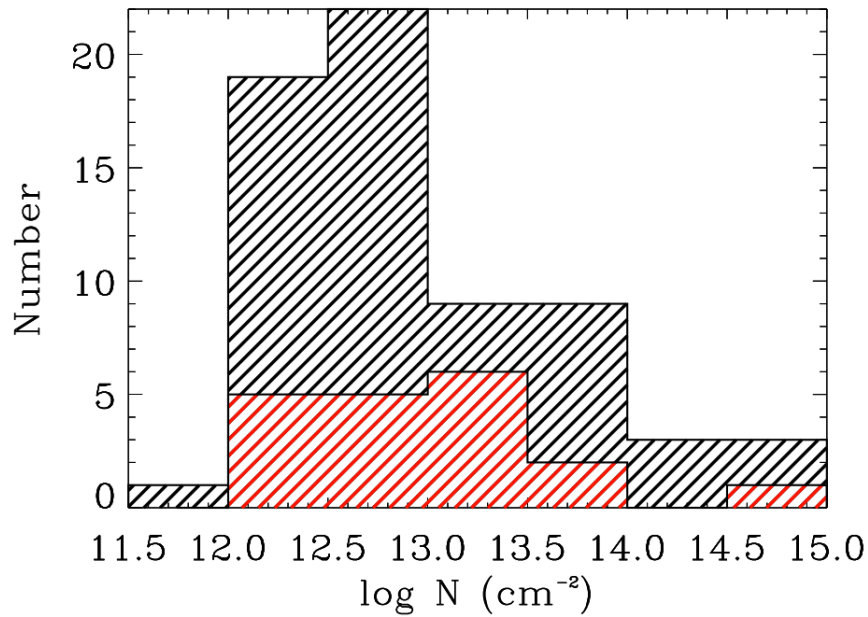


Figure 4.3: Distribution for the column densities for observed ions in the survey. Black represents the MgII distribution (62 components) while red is the FeII distribution (19 components). The bin sizes of the distribution are $0.5 \log(\text{cm s}^{-1})$.

4.4 Multi-Component Fits and Distance

Within a particular sightline, each individual absorption component represents a discrete LISM cloud. All sightlines whose spectrum we were able to fit indicated the presence of at least 1 cloud, indicating the presence of ISM in every direction.

The sightlines in this survey indicated anywhere from 1 to 5 clouds depending on galactic direction and sightline distance. As projected by the previous surveys, the number of clouds identified along a sightline is directly correlated to the length of the sightline (Figure 4.4). The distance to a sightline’s target star places an upper limit on the starting point of each cloud.

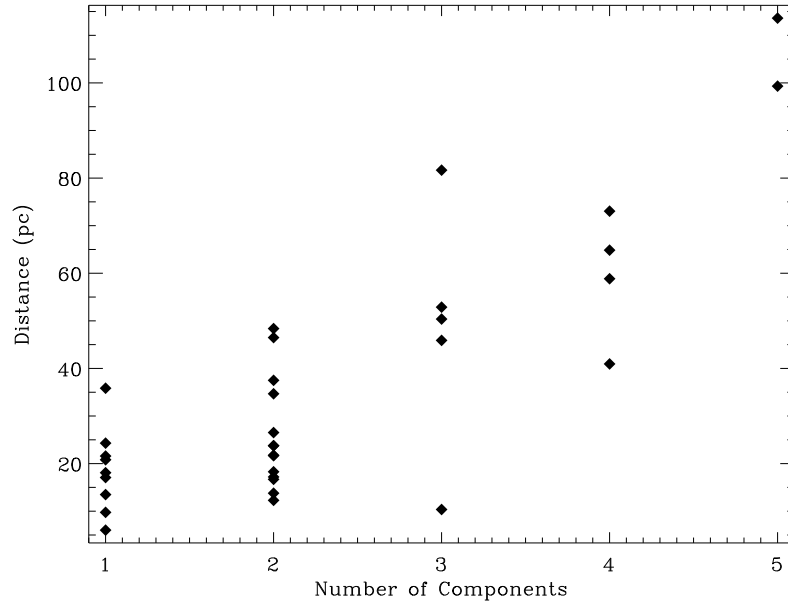


Figure 4.4: As the length of the sightline increases, the number of absorption components increases as well. This trend is consistent with the prediction that the LISM being made up of discrete clouds.

Despite this trend of increasing number of components as compared with sightline distance, this assessment does not provide a confident determination of the distribution of clouds as a function of distance. Clouds could possibly be densely clustered directly around our solar system or they could be even distributed with distance throughout the Local Bubble. The flattening of this correlation at larger sightline lengths suggests that the LISM clouds are not uniformly distributed, but rather are more densely populated closer to our solar system. Examination

of sightlines in 10 pc distance bins performed by Redfield & Linsky (2004) support the uneven distribution of clouds throughout the Local Bubble. They found their distribution remained flat after 30 pc, suggesting that the LISM clouds are more concentrated close to the solar system. Section 5.2 looks into the small scale structure of the LISM. For sightlines of close observable proximity, but different distances, an increase in number of components can further solidify the boundaries of individual clouds.

Chapter 5

Discussion

The contribution of the 34 sightline fits from this survey broadens the scope and increases the accuracy of the current dynamical model of the LISM. Due to the complexity of the LISM on a small scale, the addition of many sightlines in close angular proximity to previously studied sightlines allows for the boundaries of clouds to be more precisely defined. The large number and spread of sightlines in this survey also allowed us to probe areas of the sky that have not been investigated before and possibly identify new clouds. In addition to LISM model refinement and growth, the analysis of these sightlines motivates various other investigative paths. The column density measurements allow us to probe the depletion of particular elements onto dust grains in the clouds while the Doppler parameter can be used to determine the temperature and turbulence of clouds. Additionally, the contribution of heavy element fits of the LISM helps constrain a spectrum's HI Lyman- α (1215.67 Å) absorption which is currently the best method to detect astrospheres (Wood 2004).

5.1 Comparison to Kinematic Model

Previous to this study, 15 individual LISM clouds (Figure 1.2) have been identified within 100 pc through NUV analysis of 191 sightlines (Redfield & Linsky 2008; Malamut et al. 2014). The addition of 34 new sightlines identifying 72 in-

dividual absorption components significantly increases the sample size of LISM measurements and provides greater sky coverage. Since the correlation of multiple velocities in a given path of sky is required to solve for a single velocity vector of an LISM cloud, the increased sample also provides further constraint on each cloud's overall velocity vector.

The initial analysis of individual sightlines began with comparing spectral absorption features to the predicted LISM cloud velocities obtained from Redfield & Linsky's Kinematic Calculator (produced in conjunction with their 2008 paper). The calculator provides a list of LISM clouds a sightline traverses with corresponding radial velocities, as well as "nearby" clouds and their velocities (nearby is defined as a cloud whose boundary is $< 20^\circ$ from the given sightline). Once individual components and their corresponding velocities have been identified through the fitting procedure, they are once again compared to the predictions of the Kinematic Model. Identified clouds are considered to be a match to their prediction if their velocity is found to be within 3σ of the predicted velocity. For identified components that fall within 3σ of multiple predictions, the closer prediction is chosen. Table 5.1 presents the survey's comparison to the Kinematic model.

For many sightlines, particularly those of greater length, additional clouds were identified than the model predicted. In these cases, the additional cloud's velocity is compared to the "nearby" predictions, and often was found with a match. Matching a sightline's components to "nearby" clouds allows us to revise and further refine the boundaries of clouds. Components that find no velocity match even in nearby clouds are labeled as "NEW" and are compared to surveys more recent than (Redfield & Linsky 2008), such as (Malamut et al. 2014) to determine if they can corroborate the existence of any additional LISM clouds beyond the 15 currently identified.

Table 5.1: Comparison with Kinematic Model

HD No.	Other Name	Distance (pc)	Component No.	v (km s ⁻¹)	Cloud	Alternative Cloud
191408	HIP99461	6	1	-24.35 ± 0.50	Mic	
	GJ436	9.8	1	1.52 ± 4.3	LIC	Leo
17925	-ERI	10.4	1	9.23 ± 0.24	Blue	
			2	17.06 ± 0.41	LIC	
			3	23.94 ± 0.49	G	
37394	HIP26779	12.3	1	18.95 ± 0.17	LIC	
9826	-AND	13.5	1	13.22 ± 0.06	LIC	Hyades
166	HR8	13.8	1	2.60 ± 1.06	Eri	NEW
			2	8.85 ± 0.55	LIC	
43162	HD43162	16.7	1	11.57 ± 0.40	Blue	
			2	16.85 ± 0.24	LIC	
	WD0644+376	17.1	1	21.29 ± 0.31	LIC	
165185	HD165185	17.2	1	-28.55 ± 1.09	Aql	
			2	-23.47 ± 2.72	G	
82443	HD82443	18.1	1	12.56 ± 0.26	LIC	Leo
82558	HD82558	18.3	1	9.98 ± 0.51	Leo	LIC/G
			2	18.91 ± 0.36	Aur	
203244	HD203244	20.8	1	-9.59 ± 0.19	Vel	G
199288	HD199288	21.6	1	-19.00 ± 0.39	Vel	
116956	HD116956	21.7	1	-0.15 ± 0.08	NGP	LIC
			2	7.72 ± 0.10	NEW	
59967	HD59967	21.8	1	4.79 ± 0.39	Blue	
	GJ9124	22.1	1	13.03 ± 0.78	NEW	Aur
			2	21.94 ± 0.67	LIC	
128987	HD128987	23.8	1	-22.30 ± 0.51	G	
			2	-17.94 ± 0.57	Leo	Gem
	CD-34D7151	23.8	1	-5.49 ± 0.28	G	
			2	3.53 ± 0.22	Cet	
73350	HD73350	24.3	1	12.92 ± 0.26	LIC	
	WD0227+050	26.5	1	10.32 ± 0.91	Blue	
			2	17.55 ± 0.90	LIC	
129333	HD129333	35.8	1	-2.60 ± 0.35	LIC	
26462	HD26462	37.5	1	15.76 ± 0.51	Hyades	
			2	22.00 ± 0.22	LIC	
83443	HD23443	40.9	1	-1.59 ± 0.32	G	
			2	9.82 ± 0.94	Vel	
			3	16.66 ± 0.74	Cet	
			4	22.41 ± 0.90	NEW	
283654	HD283654	45.9	1	11.70 ± 0.40	Hyades	
			2	21.6 ± 0.40	Aur	
			3	23.43 ± 0.68	LIC	
27901	HD27901	46.4	1	21.19 ± 0.50	Aur	
			2	24.73 ± 0.42	LIC	
209458	HD209458	48.4	1	-12.39 ± 1.23	NEW	
			2	-5.07 ± 0.74	Eri	LIC
	WD2111+498	50.4	1	-18.93 ± 0.41	Oph	
			2	-11.84 ± 0.78	Mic	
			3	-3.43 ± 0.94	LIC	Aql
32008	HD32008	52.9	1	2.02 ± 0.21	NEW	
			2	11.57 ± 0.11	Hyades	
			3	20.69 ± 0.17	LIC	
	WD2211-495	58.9	1	-11.47 ± 0.52	Vel	
			2	-4.36 ± 0.52	LIC	NEW
			3	0.97 ± 0.52	NEW	
			4	6.07 ± 0.52	Dor	
240764	HD240764	64.9	1	-1.44 ± 0.58	NEW	
			2	8.1 ± 2.68	Hyades	
			3	16.69 ± 0.50	Aur	
			4	23.33 ± 1.00	LIC	
33959C	HD33959C	73.1	1	7.72 ± 0.49	Hyades	
			2	14.73 ± 0.74	NEW	Aur
			3	23.46 ± 0.86	LIC	
240764	RW Aur	81.7	1	-1.44 ± 0.58	NEW	
			2	8.10 ± 2.68	Hyades	
			3	16.69 ± 0.50	Aur	
			4	23.33 ± 1.00	LIC	
160365	HIP86373	99.3	1	-37.02 ± 1.14	NEW	Aur
			2	-34.84 ± 1.14	NGP	
			3	-27.48 ± 1.16	Mic	Oph/G
			4	-22.47 ± 1.17	G	
			5	-18.96 ± 1.18	LIC	
	BD+28D4211	113.6	1	-22.42 ± 0.52	NEW	
			2	-15.93 ± 1.46	NEW	Mic
			3	-13.26 ± 0.93	Mic	
			4	-9.31 ± 0.49	NEW	
			5	-5.69 ± 0.57	Eri	

Present in 22 of the 34 sightlines, the LIC (Local Interstellar cloud) is by far the most prominent cloud. It traverses sightlines from nearly all regions of the sky, including 4 of the shortest sightlines, indicating that it covers most of the sky and its boundary is very close to our solar system. This claim is supported by Redfield & Linsky (2008) which finds the LIC and G clouds to be the two closest clouds to our solar system. Their findings further attest that the Sun currently appears to be located in the transition zone between the LIC and G cloud. Investigations by Vannier (2020) are currently looking deeper into the transition between these clouds in order to map the Sun’s historical trajectory through these LISM clouds.

5.1.1 Previously Unidentified Clouds

Redfield & Linsky (2008) analyzed 81 sightlines whose target stars were all within 15 pc. The increased distance of sightlines covered by this survey as well as (Malamut et al. 2014) along with the increased sky coverage resulted in the identification of multiple clouds not known by Redfield & Linsky’s Kinematic Modeler. Of the 76 components that were identified in this survey, 13 were not predicted by the Kinematic Calculator; these clouds are labeled “NEW” in Table 5.1. These clouds were then compared to the “new” clouds identified by (Malamut et al. 2014) to see if there were any similarities, possibly indicating the same “new” cloud. Two of the “new” clouds identified in this survey do correspond in location and velocity to the “new” clouds identified in (Malamut et al. 2014). The component identified in HD83443’s spectrum at $22.41 \pm 0.90 \text{ km s}^{-1}$ corresponds to Malamut et al. (2014)’s identification of a “new” component in HD43940 at $22.28 \pm 0.64 \text{ km s}^{-1}$. Additionally, the “new” component unidentified in HD209458’s spectrum at $-12.39 \pm 1.23 \text{ km s}^{-1}$ corresponds to Malamut et al.

(2014)’s identification of a “new” component in HD210334 at -13.32 ± 0.03 km s^{-1} . Both sets of targets are within 30° of angular separation from each other. While 2 similar velocity measurements with this close proximity is not enough to definitively identify a new LISM cloud, it does promote the importance of further investigation into these regions of the sky.

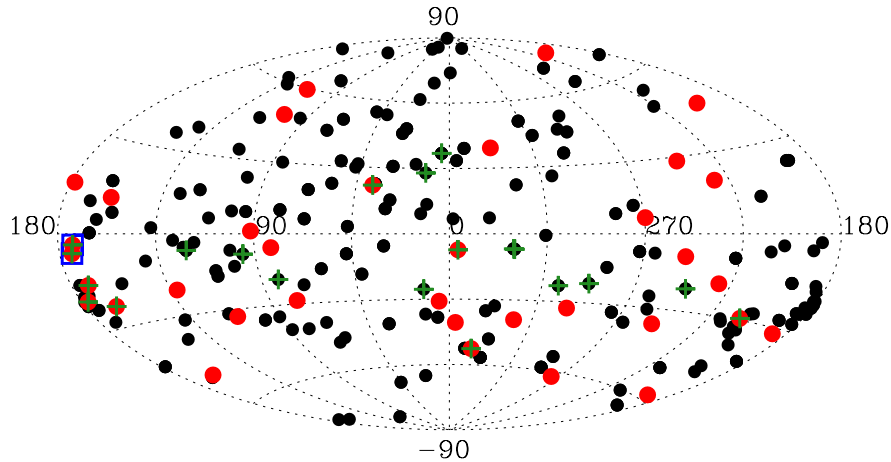


Figure 5.1: A map of all analyzed sightlines. Red points indicate sightlines analyzed in this survey. Points labeled with a green + indicate sightlines that identified “new” LISM clouds in this survey and Malamut et al. (2014). The points in the blue box are sightlines which were used to analyze the small scale structure of the LISM and whose spectra are plotted in Figure 5.2.

Malamut et al. (2014) identifies 18 “new” clouds along various sightlines, all of which were identified along sightlines that stretched 25 pc or longer. Similarly, of the 13 “new” clouds identified by this survey, 11 were identified along sightlines of at least 25 pc. This correlation presents the possible conclusion that these clouds were unidentified by (Redfield & Linsky 2008) because their boundaries do not extend to the region analyzed in that survey (within 15 pc of the solar system). However, based on their identified location in the sky, it is also possible that they were not noticed by Redfield & Linsky’s 2008 investigation because

their boundaries do not reach any of the sightlines that were previously analyzed. Figure 5.1 indicates the sightlines for which “new” clouds have been identified.

5.1.2 Small Scale Structure

As indicated by many previous studies, the LISM is not a single homogeneous cloud, but rather is made up of multiple discrete clouds (Diamond et al. 1995; Linsky & Redfield 2014). Although this model is disputed by Gry & Jenkins (2014), who argue the LISM is composed of a single cloud, the presence of multiple discrete components with high variations in radial velocity along a single sightline presents strong evidence supporting the multi-cloud model. Large changes in column densities and velocities indicating different clouds can be apparent over large scales, however determining the more precise boundaries of individual clouds as well as internal cloud structure require analysis of multiple sightlines within a small angular separation. For example, Redfield & Linsky (2001) observed 18 members of the Hyades and were able to characterize the variation in column density throughout the cloud all 18 sightlines traversed. Malamut et al. (2014) analyzed 3 pairs of sightlines that were within 3° angular separation from each other, and was able to identify upper limits to the boundary depths of 3 different clouds. In this survey, only 1 pair of sightlines are found within an angular separation of 3° of each other; an overlay of their 2 spectra can be found in Figure 5.2.

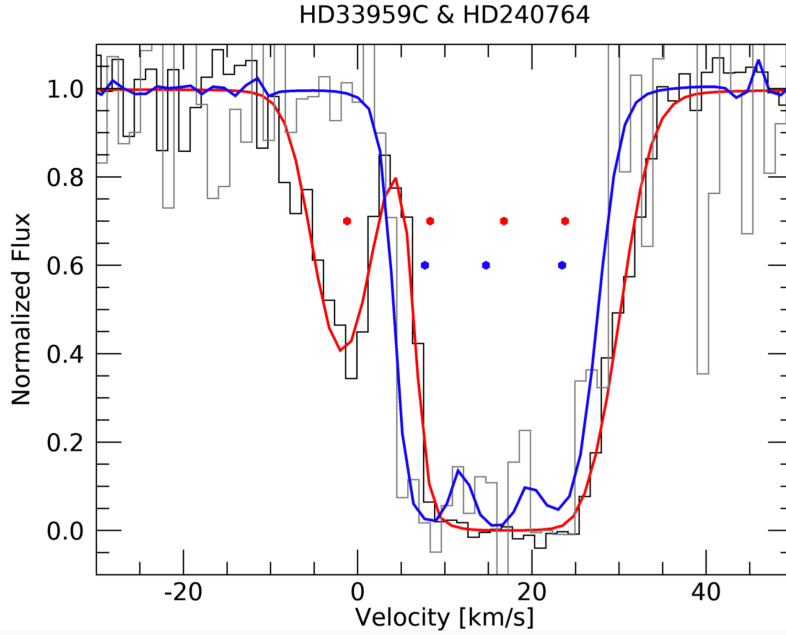


Figure 5.2: The spectra of HD33959C (blue) and HD240764 (red); the centroids of each sightline’s components are marked with a point in the color corresponding to their spectra. The solid lines denote the final fit of each spectrum’s absorption features as determined by the superposition of their individual components

HD33959C and HD240764 have an angular separation of 2.80° and distances of 81.66 pc and 64.85 pc respectively. This angular separation corresponds to 3.2 pc at the distance of HD240764. Despite HD240764’s higher saturation and slight redshift, both spectra indicate the presence of the LIC, Hyades, and Aur clouds. However, HD240764’s spectrum indicates an additional absorption feature not present in HD33959C’s spectrum. Furthermore, this additional cloud is not predicted by the Kinematic Calculator, nor does it match up with any of the “nearby clouds”. Since HD33959C is the more distant of the 2 targets, the presence of an additional cloud in HD240764’s spectrum indicates that the boundary of this unidentified cloud must be between these 2 sightlines.

Despite the fact that only 1 pair of sightlines within this survey are close enough to perform meaningful small scale structure analysis, 4 additional sightlines

in this survey are found within 3° of sightlines analyzed previously by either Redfield & Linsky (2008) or Malamut et al. (2014). These sightlines (HD199288, HD73350, HD160365, and CD-34D7151) present the opportunity to further our small scale structure analysis with the goal of more precisely defining the boundary of the clouds they traverse.

5.2 Depletion

Since the dust of the LISM is non-emissive, we are only able to observe the LISM through its absorption of stellar spectra. The abundance we obtain through our measured column density of this absorption is therefore only representative of the gas phase abundance of a particular ion. Due to its proximity, we expect the elemental abundances in the LISM to be comparable to the Solar abundance. However, the elemental abundances we obtain through our column density measurements for heavier ions falls far below the expected Solar abundance. This discrepancy can be attributed to the depletion of heavier elements onto dust grains. Depletion is calculated from

$$\log_{10}(X_{gas}/H) = \log_{10}(N(X)/N(H)) - \log_{10}X/H_{\odot}$$

where X denotes the heavy element, $N(X)$ is the column density of that element, and H is hydrogen (Jenkins 2009). Depletion is determined by calculating the ISM abundance and then subtracting the solar abundance (Wood et al. 2002). Negative deletions ($\log_{10}(X_{gas}/H)$) indicate ions that are trapped in dust while positive deletions indicate that those ions remain in the gas phase (Zachary et al. 2018). Previous LISM studies such as Redfield & Linsky (2008) and Zachary et al.

(2018) have calculated the depletion of individual LISM clouds (LIC, Oph, Vel, and Dor) using MgII column densities. The addition of the column densities from the sightlines in this survey can provide additional depletion measurements for these and other LISM clouds.

5.3 Temperature and Turbulence

The majority of the targets in our survey have been previously observed in the FUV, allowing for the spectral fit of lighter ion (like hydrogen) absorption. The Doppler parameters of the heavy ion fits found in this survey can be combined with data of lighter ion fits to disentangle the contributions of thermal and turbulent broadening for individual components along a given sightline. The equation in Section 4.2 shows the dependence of the Doppler parameter b on the cloud's temperature (T) and turbulent velocity (ξ). Lighter ions are more affected by thermal broadening than heavier elements due to its dependence on atomic mass. Knowing this, and being able to compare the Doppler parameters for absorption features of various ions along the same sightline provides us with calculations of the temperature (T) and turbulent velocity (ξ) of any traversing clouds. The calculations for T and ξ for the sightlines towards HD32008 and HD203244 have been completed (see Figure 5.3).

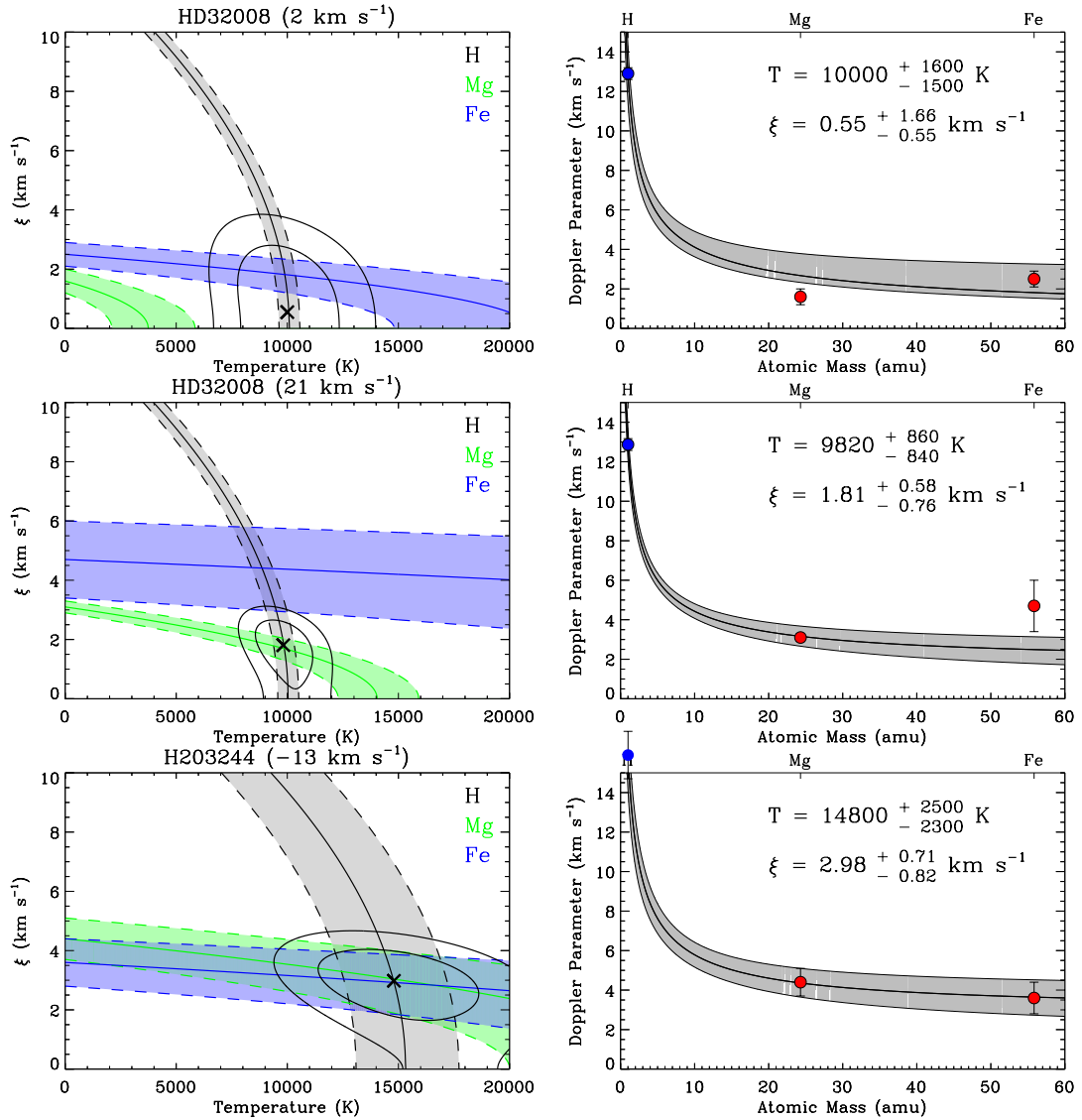


Figure 5.3: Determination for 2 of the components for the LISM absorption towards HD32008 and the component towards HD203244. The Doppler parameters for the hydrogen absorption of both sightlines' components come from Wood et al. (2005). The plots on the left represent the best-fit Doppler parameters for each ion (color coded according to the labels in the upper right-hand corners). The black × marks the best-fit T and ξ given the b values of all of the included ions. The plots on the right show the Doppler parameter plotted against atomic mass with a line of best fit shown. The best-fit values of T and ξ are presented at the top of each of these plots.

5.4 Ly α Emission and Astrospheres

Identification of the LISM around a star is crucial for the understanding of a stellar astrosphere. An astrosphere, analogous to the Sun's heliosphere, is the boundary between the outward pressure of the stellar wind and the inward pressure of its surrounding ISM. The most successful method to date to detect astrospheres is through the spectroscopic analysis of stellar HI Lyman- α (Wood 2004). However, because neutral hydrogen produces a broad, saturated absorption feature, it is often difficult to detangle the component caused by the astrosphere and the component(s) caused by the ISM using the Ly α emission alone. Figure 5.4 shows an example of a typical Ly α emission feature with a heavily saturated HI absorption.

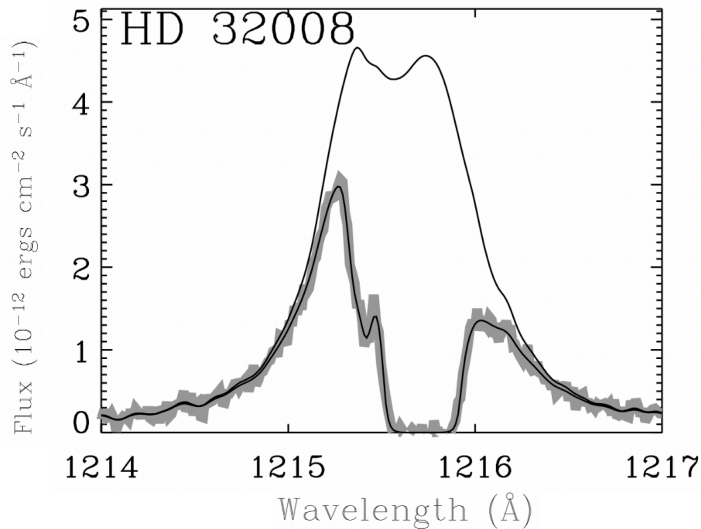


Figure 5.4: Spectrum of HI Lyman α emission of HD32008 from Wood et al. (2005). The narrower absorption feature -0.33 \AA from the central Ly line is the DI absorption, while the much broader feature is the HI absorption. The upper solid line is the reconstructed stellar Ly α emission.

Because ISM HI column densities towards even very near stars are high enough to cause extended damping wings in the stellar HI absorption, the stellar Ly α

emission must be reconstructed before the HI absorption can be analyzed (Wood et al. 2005). This is done through the process of fitting the narrower DI absorption feature and applying its component parameters to the HI absorption (assuming the same ISM clouds are causing the absorption in both cases). Figure 5.5 shows the DI fit of HD32008 from (Wood et al. 2005).

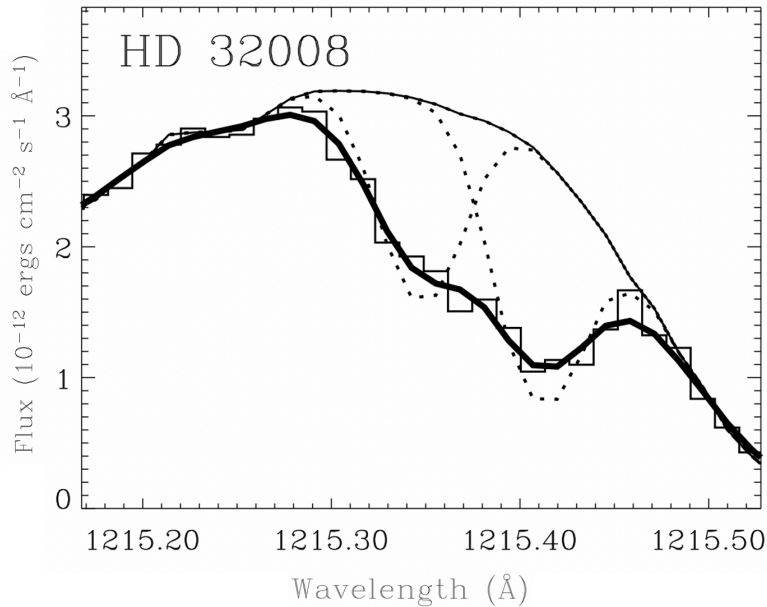


Figure 5.5: The DI absorption fit of HD32008 from Wood et al. (2005). This fit assumes 2 ISM components (denoted by the dotted lines) while the analysis of the absorption of the heavy elements in this survey indicate 4 discrete components.

Due to their even narrower absorption features, using heavier elements' emission to identify ISM components provides a more accurate measurement of the number of components and their physical parameters. The accuracy of this measurement is crucial in recreating the stellar Ly α emission. Because the identification of an astrosphere is based on the presence of stellar HI absorption, underestimating the ISM HI absorption can indicate a misleadingly high amount of stellar HI absorption. This can lead to a false positive identification of an astrosphere.

In this survey, 13 sightlines have had previous Ly α analyses with the possibility of astrospheric detection. If the number of ISM components and their parameters assumed in the stellar Ly α reconstruction is consistent with that measured from the heavier element fits (like those done in this survey), the astrospheric detection for those sightlines can be corroborated.

Chapter 6

Conclusion

The high resolution spectra of 34 stars within 100 pc indicate interstellar absorption of MgII, 18 of which also exhibit strong FeII emission that can be fit for interstellar absorption in the future. Within this survey, 62 discrete absorption features were identified in MgII and 18 in FeII, all indicative of LISM clouds. For the few sightlines where absorption was measured in multiple ion emissions, the radial velocities of particular features were consistent across each ion, arguing that the features arise due to the same clouds. The average values and distribution of final fit parameters (v_{rad} , b , $\log N$) are consistent with previous surveys of the LISM (Malamut et al. 2014; Redfield & Linsky 2002). Additionally, the trend of increasing number of components per sightline versus the distance of a sightline is also consistent with previous surveys and is indicative that the solar system is on the edge of a dense region of the LISM.

Previous studies motivating this survey (Malamut et al. 2014; Redfield & Linsky 2008) indicate that the LISM consists of 15 discrete clouds. 59 of the components measured in this survey are consistent with the LISM predictions of Redfield & Linsky (2008)'s kinematic modeler. The remaining 13 components were not predicted by Redfield & Linsky (2008) model, indicating that these components might be arising from previously unidentified clouds. Two of these “new” clouds are consistent in radial velocity and galactic location to “new” clouds identified

by Malamut et al. (2014). Although the 2 separate identifications of these “new” clouds is not enough to definitively state the clouds’ presence, it does strengthen the argument for their existence. In addition to the possible identification of new LISM clouds, the analysis of this survey helps refine the boundaries of currently known clouds. Looking more closely at the small scale structure between 2 close sightlines (angular separation of 2.8°) provides a more definitive definition of the cloud boundaries between HD240764 and HD33959C.

24 stars in this survey are found in the MAST and FUSE surveys having been observed previously in the FUV. The observation in the FUV provides analysis of ISM absorption caused by lighter elements such as H I. These observations allow for temperature and turbulence analysis of each cloud to be performed on individual clouds. Additionally, the absorption analysis of heavier ions completed in this survey motivate the further investigation of sightlines which have Ly α observations and evidence for astrospheres.

6.1 Future Work

The results from this survey further the investigation into the Local Interstellar Medium, confirming the dynamical predictions from previous surveys and increasing their precision. Although 18 sightlines exhibit FeII emission, only 5 were able to be fit at this time. The next goal for this project is to complete these FeII fits in order to corroborate the components identified by the MgII absorption. For those sightlines which do not exhibit strong enough S/N to perform independent FeII fits, upper limits on the column density will be calculated. Additionally, for those 3 sightlines which showed severely blending and saturation in MgII and were unable to be fit at this time, the next step is to apply the FeII fits as constraints

in order to obtain MgII absorption fits as well.

Combining the spectral fits from the heavy ions MgII and FeII with lighter ions from the MAST and FUSE surveys will continue to provide temperature and turbulence analysis for the identified clouds. Investigation into the small scale structure of the LISM through sightlines of this survey that are found within 3° angular separation from previously analyzed sightlines will provide further refinement into the boundaries of particular clouds. Furthermore, analyzing sightlines of various distances with similar galactic coordinates can provide more precise constraints to the depth and total column densities of individual clouds. Ultimately, incorporating additional sightlines spanning more regions of the sky will increase the accuracy and precision of the current kinematic model of the LISM and may lead to the identifications of new feature and clouds. The vast range of components' physical parameters measured in this survey exhibits the complexity of the LISM and motivates the need to attain conduct additional LISM surveys so that full-sky coverage can be obtained in order to accurately model the LISM.

Bibliography

Asplund, M., Grevesse, N., & Sauval, A. J. 2005, *Astronomical Society of the Pacific Conference Series*, Vol. 336, *The Solar Chemical Composition*, ed. I. Barnes, Thomas G. & F. N. Bash, 25

Ayres, T. R. 2010, *The Astrophysical Journal Supplement Series*, 187, 149

Beals, C. S. 1936, , 96, 661

Bostroem, K. A., & Proffitt, C. 2011, *STIS Data Handbook v. 6.0*

Breitschwerdt, D., Freyberg, M. J., & Egger, R. 2000, , 361, 303

Coleman, C., Golton, E., Gondhalekar, P., Hall, J., Oliver, M., Sandford, M., Snijders, T., & Stewart, B. 1977, *International Ultraviolet Explorer Camera Users' Guide*

Cowie, L. L., & Songaila, A. 1986, , 24, 499

Diamond, C. J., Jewell, S. J., & Ponman, T. J. 1995, , 274, 589

Edelman, E., Redfield, S., Linsky, J. L., Wood, B. E., & Miller, H. 2019, *The Astrophysical Journal*, 880, 117

Frisch, P. C., Grodnicki, L., & Welty, D. E. 2002, *The Astrophysical Journal*, 574, 834

Frisch, P. C., Redfield, S., & Slavin, J. D. 2011, *Annual Review of Astronomy and Astrophysics*, 49, 237

Frisch, P. C., Sembach, K., & York, D. G. 1990, , 364, 540

Frisch, P. C., & York, D. G. 1983, , 271, L59

Genova, R., Beckman, J. E., Molaro, P., & Vladilo, G. 1990, , 355, 150

Greenstein, J. L. 1952, Publications of the Astronomical Society of the Pacific, 64, 256

Gry, C., & Jenkins, E. B. 2014, , 567, A58

Hartmann, J. 1904, , 19, 268

Heger, M. L. 1919, , 31, 304

Jenkins, E. B. 2009, , 700, 1299

Lallement, R., & Bertin, P. 1992, , 266, 479

Lallement, R., Welsh, B. Y., Vergely, J. L., Crifo, F., & Sfeir, D. 2003, , 411, 447

Linsky, J. L., et al. 1993, , 402, 694

Linsky, J. L., & Redfield, S. 2014, , 354, 29

Linsky, J. L., Rickett, B. J., & Redfield, S. 2008, , 675, 413

Malamut, C., Redfield, S., Linsky, J. L., Wood, B. E., & Ayres, T. R. 2014, , 787, 75

McKee, C. F., & Ostriker, J. P. 1977, , 218, 148

Morton, D. C. 2003, The Astrophysical Journal Supplement Series, 149, 205

Pavlov, A. A., Toon, O. B., Pavlov, A. K., Bally, J., & Pollard, D. 2005, , 32, L03705

Preval, S. P., et al. 2019, Monthly Notices of the Royal Astronomical Society, 487, 34703487

- Redfield, S. 2009, A SNAPSHOT Survey of the Local Interstellar Medium: New NUV Observations of Stars with Archived FUV Observations, HST Proposal
- . 2013, A SNAP Survey of the Local Interstellar Medium: New NUV Observations of Stars with Archived FUV Observations, HST Proposal
- Redfield, S., & Linsky, J. L. 2001, , 551, 413
- Redfield, S., & Linsky, J. L. 2002, The Astrophysical Journal Supplement Series, 139, 439
- . 2004, The Astrophysical Journal, 602, 776
- Redfield, S., & Linsky, J. L. 2004, , 613, 1004
- Redfield, S., & Linsky, J. L. 2008, The Astrophysical Journal, 673, 283
- Savage, B. D., & Sembach, K. R. 1996, , 34, 279
- Sfeir, D. M., Lallement, R., Crifo, F., & Welsh, B. Y. 1999, , 346, 785
- Slavin, J. D., & Frisch, P. C. 2002, , 565, 364
- . 2007, , 130, 409
- . 2008, A&A, 491, 53
- Usoskin, I. G., Alanko-Huotari, K., Kovaltsov, G. A., & Mursula, K. 2005, Journal of Geophysical Research (Space Physics), 110, A12108
- Vannier, H. 2020, in American Astronomical Society Meeting Abstracts, American Astronomical Society Meeting Abstracts, 368.06
- Wood, B. E. 2004

- Wood, B. E., Redfield, S., & Linsky, J. L. 2001, arXiv e-prints, astro
- Wood, B. E., Redfield, S., Linsky, J. L., Müller, H.-R., & Zank, G. P. 2005, , 159, 118
- Wood, B. E., Redfield, S., Linsky, J. L., & Sahu, M. S. 2002, *The Astrophysical Journal*, 581, 1168
- Wyman, K., & Redfield, S. 2013, *The Astrophysical Journal*, 773, 96
- Zachary, J., Redfield, S., Linsky, J. L., & Wood, B. E. 2018, , 859, 42